

A Study of the Noise Source Mechanisms in an Excited Mach 0.9 Jet - Complementary Experimental and Computational Analysis

Rachelle L. Speth*, Michael Crawley†, Lior Gefen‡, Datta V. Gaitonde§, Mo Samimy¶ and Roberto Camus||
Mechanical and Aerospace Engineering, The Ohio State University, Columbus, OH

Coordinated experimental and numerical results are analyzed concurrently to explore the dynamics of large-scale structures and the resultant effect on the acoustic signals in a Mach 0.9 jet. The results comprise an unheated jet which is being excited by plasma actuators in order to produce coherent structures with a well-defined phase. The dynamic interactions of the generated large-scale structures are investigated using phase-averaging and iso-levels of Q-criterion. The near-field is then decomposed into its constitutive hydrodynamic and acoustic components using a spatio-temporal wavelet transform. Two-point correlations between the full and decomposed near-field, and the near- and far-field acoustic signals are utilized to identify the dominant acoustic source regions in both jets. Our previous experimental work had shown that each individual actuation event produced a temporally and spatially localized pressure fluctuation in the irrotational near-field, which was termed the impulse response of the jet. The response of the jet to periodic excitation could be reconstructed from a linear superposition of this impulse response. Results also showed that the near- and far-acoustic fields are also governed by this quasi-linear mechanism (though this does not imply that the noise generation process itself is necessarily linear). Analysis of the numerical results found that this same principle applied inside the jet shear layer (at jet lipline), albeit with less accuracy; suggesting that the structure interactions are largely linear in nature.

I. Introduction

Engine exhaust constitutes one of the major components of aircraft noise during takeoff and landing, and hence poses a significant health concern for community and military personnel. Mitigation of the aeroacoustic noise generated by free jets is therefore a necessity for both the commercial and military aviation industries. Current noise reduction technologies involve high bypass engines or geometric modifications to the nozzle (e.g. tabs, chevrons, and lobed mixers). Though effective, these have associated performance penalties in terms of added weight, drag, or loss of thrust - penalties that are incurred over the entire duration of the flight due to the passive nature of the control technology. A shift to active control technology is thus desirable in order to minimize the performance penalties while maximizing the noise reduction. However, the proper application of control is not readily apparent. In the simulated two-dimensional shear layer of Wei & Freund¹ a generalized actuator was able to reduce the noise along a prescribed line in the acoustic field by up to 11 dB. The researchers observed that the excitation was not altering the broad characteristics of the shear layer (such as turbulent kinetic energy) or even the initial evolution of the most energetic structures in an appreciable manner. Rather, the control appeared to be affecting the acoustic field by regularizing the large-scale structures, thereby reducing the radiating efficiency of the noise sources. Clearly, fundamental

*Graduate Research Assistant. Student Member, AIAA

†Graduate Research Assistant. Aerospace Research Center. Student Member, AIAA

‡PhD candidate, Università Roma TRE, Dipartimento di Ingegneria, Via della Vasca Navale, 79, 00146 Roma, Italia

§John Glenn Chair Professor. Fellow, AIAA

¶John B. Nordholt Professor. Aerospace Research Center. Fellow, AIAA

||Full professor, Università Roma TRE, Dipartimento di Ingegneria, Via della Vasca Navale, 79, 00146 Roma, Italia

understanding of the noise sources and radiating mechanisms is required for efficient and effective active noise mitigation strategies.

Perhaps the most well-known source model for jet mixing noise is the two-component model of Tam *et al.*,² which recognized that the acoustic far-field spectra of jets can be represented as two distinct universal similarity spectra, irrespective of jet Mach number or temperature ratio. In this model, the incoherent fine-scale mixing layer turbulence produces an incoherent, broadband acoustic field and is believed to be the dominant source of acoustic radiation at sideline angles. In contrast, aft angle radiation is dominated by the large-scale structures and exhibits a strong spectral peak. The spectra in between are combinations of the two, with a gradual shifting from one to the other. Theoretical analysis by Tam³ demonstrated Mach wave radiation emitted through the supersonic convection of these large scale structures - the oft-mentioned "wavy-wall" analogy. This analysis was extended in Tam & Burton⁴ to include amplification and decay of the structures, through which subsonically-convecing structures were found to emit noise (this structure evolution was also shown to broaden the directivity and frequency bands of the acoustic radiation). Experiments utilizing direct correlations between density and velocity fluctuations in the shear layers of high-speed jets and the acoustic far-field have supported this two-component source model.^{5,6}

The recognition that the large-scale structures are the dominant noise sources in the turbulent jet is beyond doubt at this point. Yet, the exact dynamics that govern the evolution of the structures and ultimately the noise emission are still not fully understood. The intermittent nature of the structures and noise emission was first observed by Hileman *et al.*⁷ in a supersonic jet. Simplified source models utilizing temporally and spatially modulated wavepackets were found to reproduce the superdirective character observed in the far-field spectra, as well as improve the match between the observed and predicted spectral amplitudes.^{8–10} Hence, understanding the exact spatiotemporal evolution of the large-scale structures is important to predicting and ultimately controlling their radiation production.

The ability to perturb the jet shear layer, in effect controlling the temporal and azimuthal frequency content of the large-scale structures, may thus serve as a useful tool for noise source analysis. Localized arc-filament plasma actuators (LAFPAs) have been developed at the Ohio State University for use in high-speed flow control applications. Unlike traditional acoustic drivers, LAFPAs have been shown to produce high amplitude and high frequency excitation signals suitable for controlling the shear layer development of high Mach number and high Reynolds number jets.^{11–14} These actuators have successfully been used for both mixing enhancement and noise mitigation in laboratory scale subsonic and supersonic jets; a review of the development of LAFPAs and their use in high-speed jet flow control can be found in Samimy *et al.*¹⁵ In addition to their noise mitigation and mixing enhancement potential, LAFPAs have been used as diagnostic tools for understanding the large-scale structure dynamics and noise production mechanisms in high-speed jets. Kearney-Fischer *et al.*¹⁶ utilized a phase-locked schlieren imaging system to LAFPA excitation in a heated, subsonic jet in order to study the Mach-wave-like compression waves generated by the large-scale structures. By varying the frequency and Fourier mode of the forcing, the effect of structure characteristics on the radiated noise was evaluated. Sinha *et al.*¹⁷ investigated the dynamics of large-scale structure interactions in a Mach 0.9 jet by phase-averaging the near-field pressure signals from a linear microphone array. It was found that for low to moderate forcing Strouhal numbers ($St_{DF} < 0.5$), each excitation pulse produced a single structure, the near-field signature of which was a compact waveform. The waveform shape and amplitude at moderate forcing Strouhal numbers were found to be well-predicted by a linear superposition of the impulse response of the jet to excitation ($St_{DF} < 0.1$). This analysis was extended to the acoustic near- and far-field in Crawley *et al.*,¹⁸ in which it was found that the acoustic field could also be represented as a linear superposition of the impulse response of the jet.

A comprehensive closely linked computational effort is being performed at the High Fidelity Computational Multi-Physics Laboratory (HFCMPL) to analyze the effect of LAFPA-based excitation. Several detailed studies have shown that the simulations accurately capture the main qualitative and quantitative features of the experiment, including flow visualizations, mean and fluctuating data. The simulations and experiments have been leveraged to generate insight into the connection between jet turbulence and the near acoustic field. In the recent studies of Speth and Gaitonde,^{19,20} the LAFPAs were pulsed at low frequencies to analyze the impulse response and at relatively higher frequencies ($St_{DF} > 0.15$) to study the manner in which the structures begin to interact. The large coherent structures of the jet were linked to the near field through analysis of phase-averaged waveforms and correlations, which described the development and interaction of subsequent structures in time and space. The higher frequency of excitation tested ($St_{DF} = 0.25$) created a narrower correlated region than the low frequency cases due to the organized development and

decay of the large scale structures. This region extended from the end of the potential core to the 30 degrees near field. Compressibility effects were also investigated in Speth & Gaitonde²⁰ and found that the supersonic case has higher correlations throughout the near field than the subsonic cases.

The current work continues the synergistic experimental-computational effort by exploiting the relative strengths of each method (e.g., long time traces for experiments and simultaneous space-time data in the computations). Particular emphasis is placed on the evolution of large scale structures generated by forcing and the acoustic component of the near field response. The specific cases considered by both experiments and simulations are with a Mach 0.9 jet at Reynolds number of 6×10^5 , subject to $m = 0$ (axisymmetric) excitation at $St_{DF} = 0.05, 0.15$ and 0.25 . No control results are also introduced to highlight the main effects. First, the experimental and computational setups are described in Sections II.A and II.B, respectively. Then, the evolution of the large scale coherent structures is analyzed in Section III.A followed by the connection between these large scale structures to the hydrodynamically dominated nearfield in Section ???. Then the connection between the near jet region to the acoustically dominated nearfield is considered. Finally, the connection between the nearfield to the farfield signal is determined.

II. Methodology

II.A. Experimental Setup

Experimentation was conducted in the free jet facility (a schematic of which can be found in Fig. 1) at the GDTL within the Ohio State University's Aerospace Research Center. The dimensions of the chamber are 5.14 m wide by 4.48 m long and 2.53 m high (wedge-tip to wedge-tip). The design of the chamber produces an anechoic cutoff frequency of 160 Hz, which is below the frequencies of interest for this study. Additional details of the facility design and validation can be found in Hahn.²¹ Compressed, dried, and filtered air is supplied by two cylindrical storage tanks with a total capacity of 43 m^3 and maximum pressure of 16 MPa; the tanks are charged by three, five-stage reciprocating compressors. The air enters the facility horizontally, passes through a stagnation chamber and turbulence screens, and exhausts through a converging nozzle. Opposite the nozzle, a collector accumulates the jet and entrained air and exhausts to the outdoors.

A converging, axisymmetric nozzle with exit diameter of 25.4 mm was used in the current study. The internal contour of the nozzle was designed using a fifth order polynomial. The nozzle utilized a thick-lipped design in order to simplify the mounts for the LAFPA extension, which housed the eight actuators used in this study. For the experiments reported in this paper, the jet was operated with a total temperature ratio of unity. This results in a Reynolds number based on the jet exit diameter of 6.2×10^5 ; previous investigations using hot-wire anemometry have indicated that the initial shear layer is turbulent for this operating condition with momentum thickness 0.09 mm and boundary layer thickness 1 mm.²²

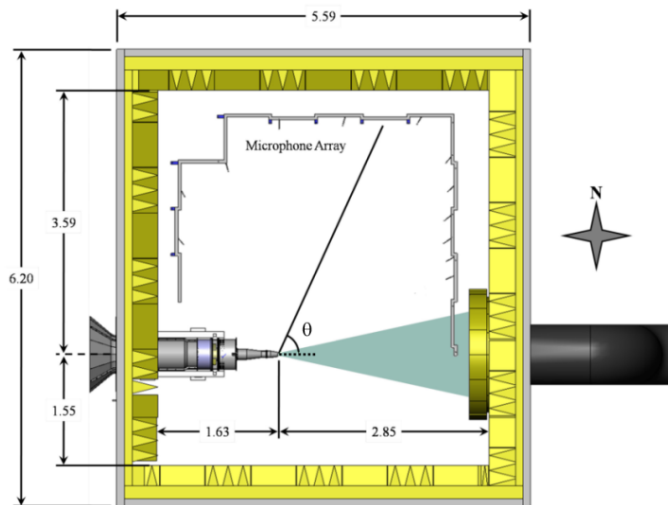


Figure 1: Plan view of GDTL free jet facility and anechoic chamber; dimensions in meters.

Excitation was applied to jet shear layer via eight LAFPAs which were uniformly spaced around the nozzle perimeter 1 mm upstream of the nozzle exit. Each LAFPA consists of a pair of tungsten pin electrodes with tip spacing (center-to-center) of 4 mm. The electrodes are housed in a boron nitride extension attached to the end of the nozzle. A more detailed description of LAFPA characteristics can be found in Utkin et al.²³ The LAFPAs are energized by a multi-channel, high-voltage plasma power generator capable of simultaneously powering up to eight LAFPAs, which was designed and built in-house at the GDTL. In the second-generation power supply, each individual circuit consists of a switchable capacitor in line with a high voltage transformer; the arcing electrodes are connected to the secondary side of the coil. The switches are controlled by a 16-channel digital I/O card and National Instruments' Labview software, operated by a dedicated computer. The plasma generator provides independent control of the frequency, duty cycle/pulse width, and phase of each individual actuator (though at a constant amplitude of 5 kV). The pulse width was held constant at 7 μ s, which was found to be the minimum pulse width at which the actuators consistently arced for all frequencies explored in this study.²⁴

Near-field and far-field pressure measurements were acquired simultaneously, using Brüel & Kjær 1/4 inch 4939 microphones. The signal from each microphone is band-pass filtered from 20 Hz to 100 kHz using a Brüel & Kjær Nexus 2690 conditioning amplifier, and recorded using National Instruments PXI-6133 A/D boards and LabView software. The microphones are calibrated using a Brüel & Kjær 114 dB, 1 kHz sine wave generator. The frequency response of the microphones is flat up to roughly 80 kHz, with the protective grid covers removed. Voltage signals are collected at 200 kHz with 81920 data points per block; sub-blocks of 8192 data points were used when calculating short-time power spectral densities, resulting in a frequency resolution of 24.4 Hz. Ten blocks were recorded for each case, resulting in four seconds of data. Analysis of the far-field acoustic spectra found this length to be sufficient for statistical convergence of the turbulence statistics.

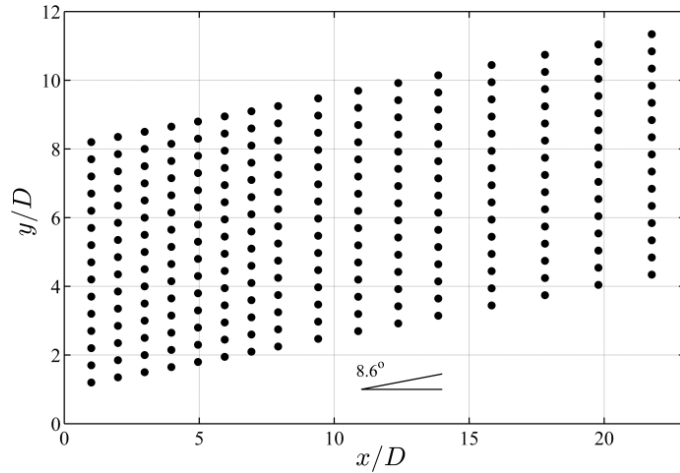


Figure 2: Near-field microphone array grid.

Far-field acoustic pressure is acquired at three polar angles: 30°, 60° and 90°, as measured from the downstream jet axis. The radial distance of the microphones ranges from 101D at 30° to 145D at 60°. The near-field pressure was acquired using a linear array of sixteen microphones located along the meridional plane of the jet; the spacing varied along the array from 1D to 2D (Fig. 2). The linear array is mounted to a traverse system at an angle of 8.6° to the jet axis in order to match the spreading angle of the jet shear layer for this Mach number.²² The traverse is controlled using LabView and enables the acquisition of pressure measurements at various radial positions with respect to the jet axis. Initially, the most upstream microphone is positioned at $x/D = 1$ and $r/D = 1.20$, to ensure that the microphone tips are outside the mixing layer and do not affect the flow field. For subsequent cases, the microphone array is incremented radially outward by 0.5D for a total travel distance of 7D. Signals from the near-field array are preprocessed in order to remove actuator-self noise while retaining the true hydrodynamic and acoustic response of the jet. This has been accomplished via a filter operating in the continuous wavelet domain. Further details may be found in the work of Crawley *et al.*¹⁸

II.B. Computational Method

The simulations employ the same approach as previously used to successfully simulate Mach 1.3 and 0.9 jets without and with control.^{20,25,26} The full compressible Navier-Stokes equations are solved in curvilinear coordinates (ξ, η, ζ) using the strong conservative form.^{27,28} The transformed non-dimensional equations in vector notation are given as:

$$\frac{\partial}{\partial \tau} \left(\frac{\vec{U}}{J} \right) + \frac{\partial \hat{F}}{\partial \xi} + \frac{\partial \hat{G}}{\partial \eta} + \frac{\partial \hat{H}}{\partial \zeta} = \frac{1}{Re} \left[\frac{\partial \hat{F}_v}{\partial \xi} + \frac{\partial \hat{G}_v}{\partial \eta} + \frac{\partial \hat{H}_v}{\partial \zeta} \right] \quad (1)$$

where $\vec{U} = \{\rho, \rho u, \rho v, \rho w, \rho E\}$ denotes the solution vector and $J = \partial(\xi, \eta, \zeta, \tau) / \partial(x, y, z, t)$ is the transformation Jacobian. Details of the various terms in Eqn. 1 may be found in Speth and Gaitonde.²⁹ For the inviscid terms, a third-order upwind biased approach is adopted, together with the Roe scheme³⁰ for flux evaluation. The limiter required to enforce monotonicity is a crucial component of the method. The van Leer harmonic limiter³¹ has proven to be very successful at reproducing the main features of the unsteadiness in the jet. The viscous terms are discretized with second-order centered differences and time integration is performed by a second-order diagonalized³² approximately factored method.³³ A sub-iteration strategy is used to minimize errors due to factorization, linearization and explicit boundary condition implementation.

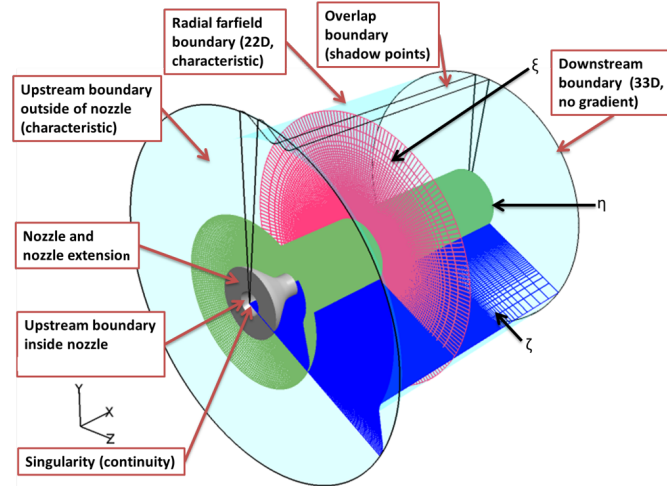


Figure 3: Computational domain

A 65 million point mesh (Fig. 3) is used to simulate the Mach 0.9 jet measured in the experiment (Fig. 1). The grid has dimensions of 685 points on the ξ (streamwise) direction, 455 points in the η (radial) direction, and 209 points in the ζ (azimuthal) direction. In the radial direction, the mesh is refined in the nozzle region and gradually stretched in the far field. At the exit of the nozzle, the grid maintains a constant axial spacing until after the potential core length; then stretches in the streamwise direction. To preserve continuity, the grid has a five point overlap in the ζ direction. Characteristic boundary conditions³⁴ are applied to the upstream (outside the nozzle) and radial boundaries. Non-reflecting conditions are applied to the downstream and far-field boundaries. Stagnation conditions are specified at the first ξ plane of the nozzle ($\rho_{inlet} = 2.04 \text{ kg/m}^3$, $U_{inlet} = 22 \text{ m/s}$, $P_{inlet} = 171,427 \text{ Pa}$) to achieve perfectly expanded nozzle exit conditions corresponding to $\rho_{jet} = 1.404 \text{ kg/m}^3$, $U_{jet} = 285.99 \text{ m/s}$, $T_{jet} = 251.31 \text{ K}$ which are similar to the experiments. Based on the nozzle diameter therefore, the Reynolds number is $Re = 635,308$. The nozzle geometry resembles that of the experiments including the nozzle ring on which the actuators are mounted. The velocity profile at the entrance to the nozzle is that of a uniform flow (zero at the wall and U_{inlet} everywhere else). Perturbations were not introduced into the inflow due to the unknown perturbations in the experiment. Therefore, the simulations have a laminar boundary layer at the nozzle exit while the experiments have a very thin turbulent boundary layer (the momentum thickness has been estimated to be 0.09mm). Previous studies have shown that despite this difference, the main features of the experimental observations are successfully reproduced by the computations by a fixed longitudinal coordinate shift to account for the

difference in the inlet characteristics of the experiment and computation.^{25,26} Other studies have shown that a smaller 32 million point simulation is adequate to reproduce the features of the experiment.¹⁹

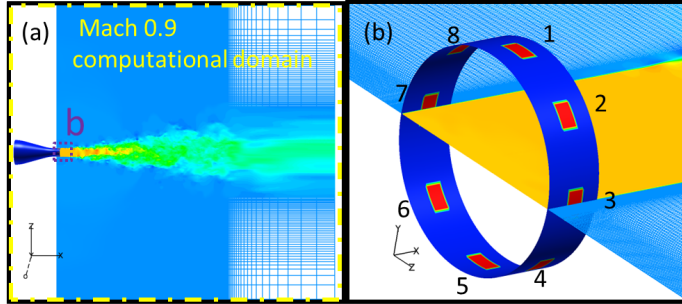


Figure 4: The computational domain including the nozzle (a), and the numerical actuator model (b)

The LAFPAs are modeled after the experiments using a surface heating technique to excite jet shear layer instabilities and azimuthal modes within the jet. Eight actuators are placed around the periphery of the jet on the nozzle collar at the locations and dimensions of the experiments as explained previously. As shown in Fig. 4b, each actuator consists of a heated region of the nozzle wall which extends the azimuthal length corresponding to the separation distance between electrodes (3mm) and has an axial extent equal to the length of the groove (1mm). The temperature of the nozzle wall was assumed to be $1.12T_{\infty}$. When the actuator is on the temperature of the actuator region increases to $5T_{\infty}$. Little difference was seen in the previous work (Speth and Gaitonde³⁵) for the temperature range measured in experiments (Utkin *et al.*¹²) for a Mach number of 1.3. The semi-empirical model is necessary to avoid first-principles simulation of the poorly understood plasma heating process, as well as to restrict the required computational resources to feasible levels (see Ref. 36).

Unlike acoustic drivers, the LAFPAs are on-off devices and thus can be represented by rectangular pulses with a duty cycle, which allows for a wide range of operation choices. Duty cycle is the percentage of actuator on time in an excitation cycle. Therefore, a duty cycle of 100% results in the actuator being on all the time. The experimental duty cycle varies with frequency, since the arc strike lasts a fixed time. Since the actuator model is empirical, the computational duty cycle was chosen to obtain similar control authority as in the experiment. This necessitates a higher duty cycle (10%) than the one used in the experiments (2.0% for $St_{DF} = 0.25$). As noted earlier, despite the simplicity of the model, its success has been documented in Gaitonde and Samimy,²⁵ where, in addition to coherent structures, mean and fluctuating quantities have been compared. Furthermore, the mean flow structure with control was shown to match the theoretical predictions of Cohen and Wygnanski.³⁷

Due to the required amount of computational time, the number of excitation Strouhal numbers was reduced from the experimental set to a select number of interesting cases. The Strouhal numbers studied in the simulations include: 0.05, 0.15, and 0.25. Data was acquired every timestep at the point probes depicted in Fig. 2 as well as on several ξ , η , and ζ computational planes. Phase-averaged data were also computed for each of the simulations.

II.B.1. Grid Resolution Study

The variations due to grid resolution are depicted in Figure 5. Figure 5a depicts the mean axial velocity along the centerline. Figure 5a compares the three grids for the Mach 0.9 case with axisymmetric excitation. The three grids, are relatively similar although G1 has a slightly higher decay rate after the potential core. However, grids G2 and G3 exhibit the same decay rate after the potential core for the extent plotted.

Figure 5b depicts the root-mean-square (RMS) fluctuating axial velocity along the centerline of the jet. The relative shape and amplitude of the fluctuating velocities is the same for each grid. Therefore, there is a very small effect in terms of the principal coherent features and jet core length, but modest sensitivity was evident. This is to be expected in implicit large eddy simulation in which no subgrid model is used. Due to the concern of nearfield wave propagation grid G3 will be used.

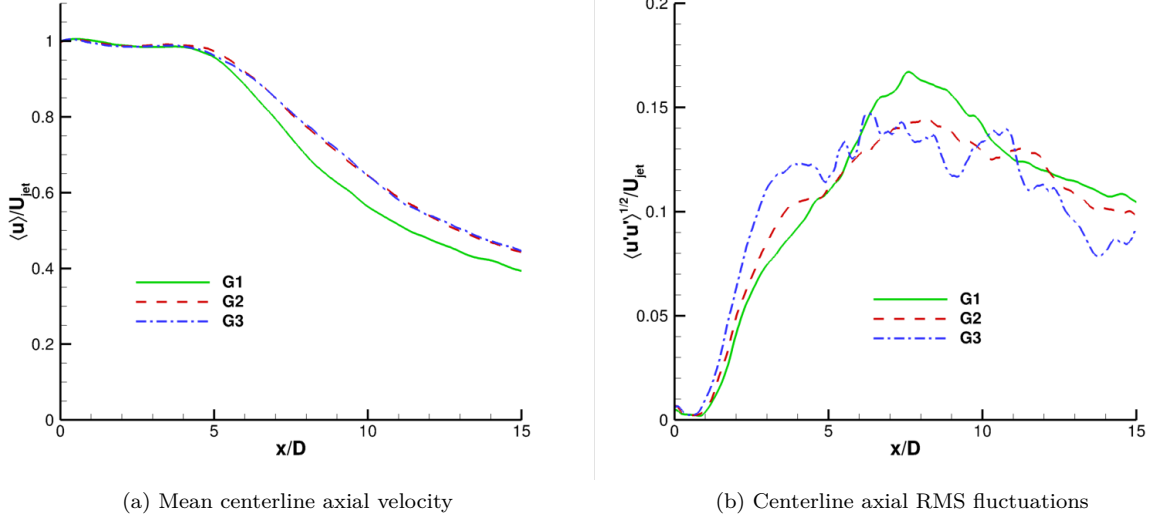


Figure 5: Grid convergence along the centerline of the Mach 0.9, $m = 0$, $St = 0.15$ case

II.B.2. Numerical Validation

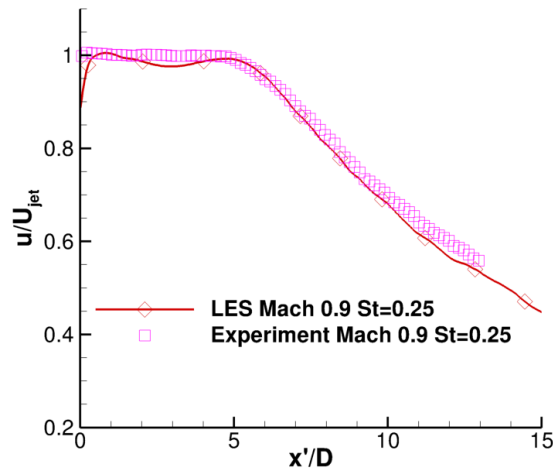
To begin, the computations will be compared to experimental results of Crawley *et al.*³⁸ These comparisons will prove not only that the schemes used for the simulations capture the physics of the flow but also the actuator model is able to produce structures similar to the experiments.

To begin, the flow will be compared in the mean sense. The time-averaged streamwise velocity and RMS fluctuations along the centerline for the natural jet are depicted in Fig. ???. The simulation data was shifted to account for the unknown turbulence in the experimental nozzle boundary layer. The boundary layer of the experiments is known to be thin and turbulent.³⁹ For simplicity and grid conservation, perturbations are not employed in the nozzle/nozzle ring. Instead a uniform flow field is applied to the first axial plane. This allows for a natural laminar boundary layer to form due to the computation of the whole nozzle. To account for the differences in nozzle exit conditions, the un-controlled jet was shifted 1.4 D downstream to match the potential core length. The effect of the boundary layer thickness is discussed by Speth and Gaitonde ???. The perturbations within the nozzle affect the dynamics of the jet as shown by Bogey *et al.*⁴⁰

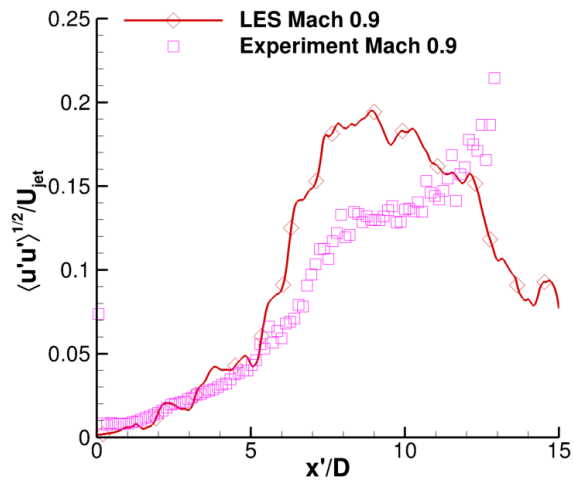
The decay rates of the mean velocity after the potential core are similar and match well. Since no turbulence is added to the simulations within the nozzle/nozzle ring, the fluctuations start at zero (unlike the experiment). The fluctuations grow at the same rate for the experiment and the simulation throughout the potential core. Beyond the potential core, the simulations has a maximum RMS value around $x/D = 8$ which corresponds to downstream of the potential core ($x/D = 6$).

The simulations reproduce the effect of the actuation in the mean sense as shown in Figure 7 for the $St = 0.25$ cases. The simulation data for Figs. 7a and b were shifted axially by $0.84D$ to match the core length of the experiment. The decay rate of the centerline axial velocity for the simulation matches the experimental rate similar to the no-control results. Figure 7b depicts the axial RMS fluctuations along the centerline for the excited case. The simulation has similar values to the experimental results throughout the axial extent shown.

When the jet is excited with the plasma actuators, large scale structures develop in the shear layer and propagate downstream. For the axisymmetric mode, ring structures form that show up as vertically aligned vortices in cross-sectional slices as shown in Fig. 8. This figure depicts the phase-averaged contours of Galilean streamlines with the background colored by axial velocity for both the experiments and the computations. Galilean streamlines are formed by subtracting the convective velocity ($U_{convect} \approx 0.65U_{jet}$) from the velocity field of the instantaneous or in this case phase-averaged snapshot. The simulations were shifted to match the potential core length of the experiments due to the unknown boundary layer properties at the exit of the nozzle extension. Even with the difference in initial turbulence level, both experiments

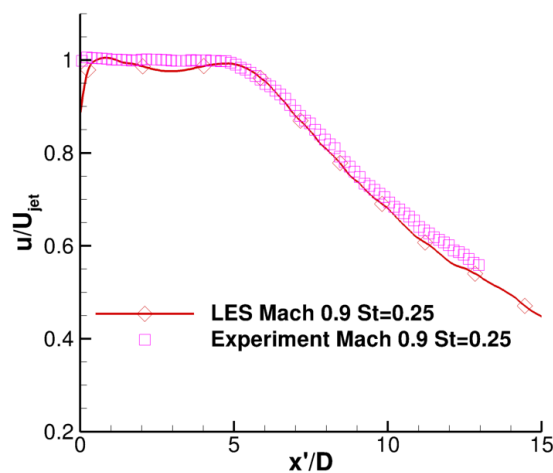


(a) Mean centerline axial velocity

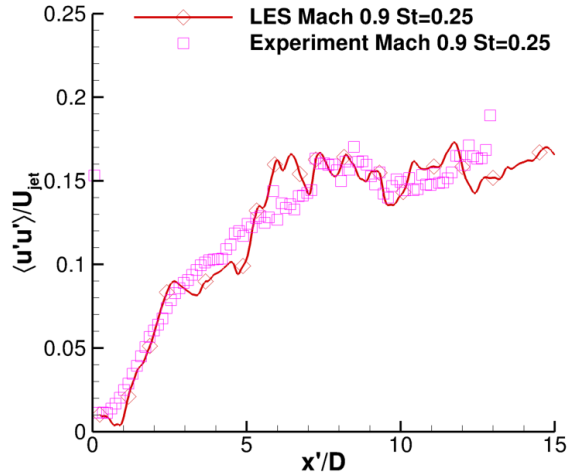


(b) Centerline axial RMS fluctuations

Figure 6: Non-dimensional mean and RMS centerline velocities for the uncontrolled jets



(a) Mean centerline axial velocity



(b) Centerline axial RMS fluctuations

Figure 7: Non-dimensional mean and RMS centerline velocities for the jets controlled with the axisymmetric mode at a $St = 0.25$

and computations have 4 distinct vortical rings before the end of the potential core signifying that the large scale structure dynamics are the same.

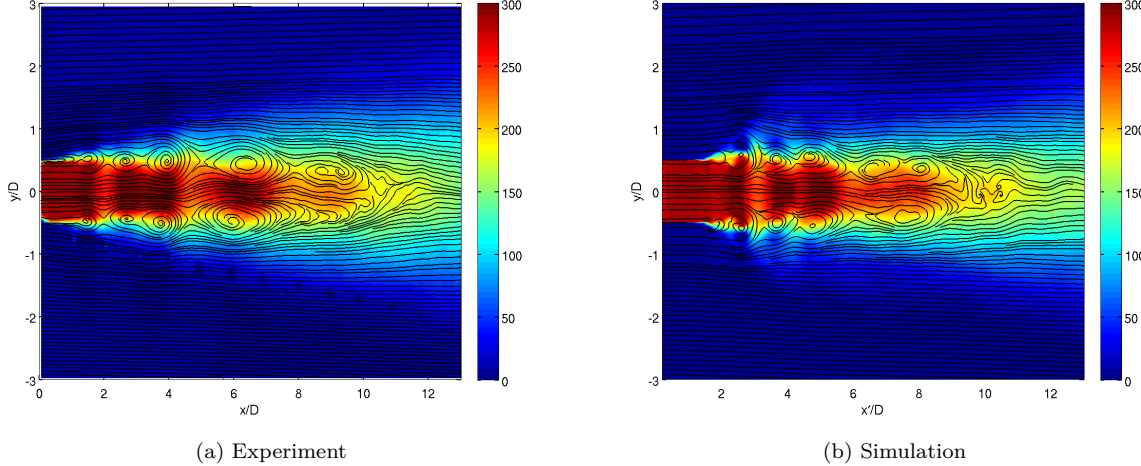


Figure 8: Phase-averaged structures highlighted by Galilean streamlines for the axisymmetric mode at a $St = 0.25$

The coherent structures that develop in the jet (Fig. 8) affect the near field and thereby the sound generation. The nearfield noise propagation of the simulations will now be shown to be the same as the experimental results obtained along the probe arrays of Fig. ???. Figure 9 depicts the instantaneous gauge pressure of the $St = 0.25$ forced simulation and experiment located at $x/D = 2$ on *Array 1*. Also shown is the simulation actuator temperature profile versus time. The simulation pressure was divided by a factor of 2.3 in order to match the experimental wave amplitude. The amplitude of the pressure waves are highly dependent on pressure probe location accuracy, actuator location, nozzle lip width, and nozzle exit boundary layer conditions making it difficult to match quantitatively.¹⁷ Qualitatively, the experimental pressure depicts a sharp discontinuous region ($t = 0.01113s$ and $0.01165s$) before a pressure wave (extremas located at $t = 0.01114s$ and $0.01118s$) consisting of a peak followed by a trough. The discontinuous region is associated with the actuator self-noise while the pressure wave is associated with the large scale structure generated by the actuator perturbation. The self-noise is a compression wave generated by the actuators that moves at the speed of sound and can be seen in the near field. In the simulation, the discontinuous region is not present. Instead, there is a small secondary peak in the upward rise of the pressure wave. Since the effect of the actuators is modeled, the shock-like structure that occurs in the experiment is not captured. The effect of the actuators on the dynamics of the jet is captured however.

To further convey that the dynamics of the nearfield are captured, Fig. 10 plots the phase-averaged waveforms for the experiment and simulation on *Array 1* for a $St = 0.25$. Observe that the effect of the actuator self-noise seen in the experimental data diminishes with axial distance. The trends for the growth and decay of the experimental waves are the same as the simulations. These trends include: sine-like waveforms by $x/D=2$, increases in the waveform amplitude with axial distance within the potential core, and decay in amplitude of the periodic waves but maintain sine-like shape far beyond the potential core. This reduction in amplitude beyond the potential core is due to the break up of the large scale structures created by the excitation.

III. Results

III.A. Evolution of the Large-Scale Structures

The majority of the sound heard in the downstream angles is due to the coherent structures developed in the shear layer. Therefore, to begin, the formation and decay of these structures will be analyzed. The phase-averaged isolevels of Q-criterion ($Q = 0.35$) colored by axial velocity with a background of dilatation in gray scale are illustrated in Figs. 11 through 13 for each excitation case. Each figure depicts two phases of

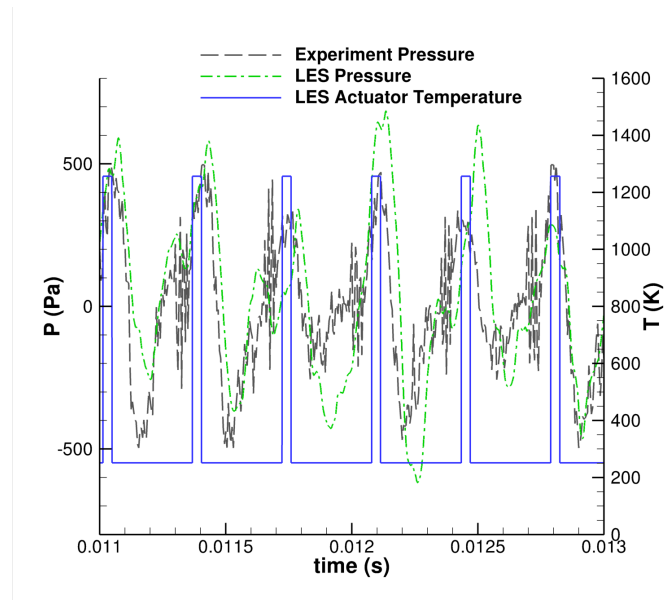


Figure 9: Near field pressure response for the $St=0.25$ forced Mach 0.9 jet and the actuator temperature at $x/D = 2$ on *Array 1* with experimental results³⁸

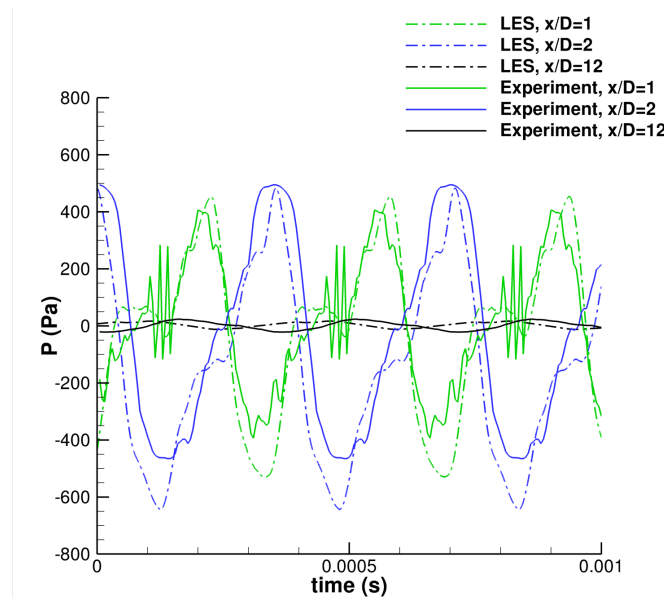


Figure 10: Phase-averaged waveforms on *Array 1* for experiment³⁸ and LES with $St=0.25$ excitation for Mach 0.9

the excitation period ($\phi = 0.1(2\pi)$ and $0.6(2\pi)$). In each phase, the locations of $x/D = 2$ and 4 of *Array 1* (array locations shown in Fig. 2) are labeled. For all cases, small individual vortical rings are produced near the nozzle exit by the break down of the shear layer. As these vortical rings move downstream they become bigger for the two higher frequencies. This is accompanied by the spreading of the jet due to entrainment. This is not readily seen in the phases depicted for the low frequency case due to the structure already having convected out of the viewing area. As discussed in Sinha *et al.* [Cite Ani PoF 2012], the characteristic frequencies of the structures generated by very low-frequency excitation ($St_{DF} < \sim 0.1$) are much higher than the excitation frequency itself. Hence, in this excitation regime, the excitation phase does not necessarily correspond to phases in the life-cycle of the individual structure generated by an excitation event. At the higher frequencies, streamwise ribs connecting successive rings are also evident:²⁵ these represent increasing interaction between successive rings. These connect the outer part of one ring to the inner part of the previously generated structure, where the velocity is higher. The subsequent decay of the large structures is clearly evident. At any given location, the degree of prominence of the rollers depends on the phase: for example, in the $St = 0.15$ case, there is a well formed roller at about $x/D = 4$ at $0.1(2\pi)$ phase but at $0.6(2\pi)$ the roller is broken down at the same axial location. Similar effects can be seen in the phase averaged results for the $St = 0.25$ case. Another feature of the flow is the presence of hair-pin like structures, which are especially prominent in the higher frequency cases: note for example the structure at $0.6(2\pi)$ for $St = 0.25$ slightly before the $x/D = 2$ probe. For the $St = 0.05$ cases (Fig. 11), the A' and A structures are depicted in the phase $0.1(2\pi)$. At the phase of $0.6(2\pi)$, the structure in the first phase has already broken up resulting in no observable actuator induced structures in this phase.

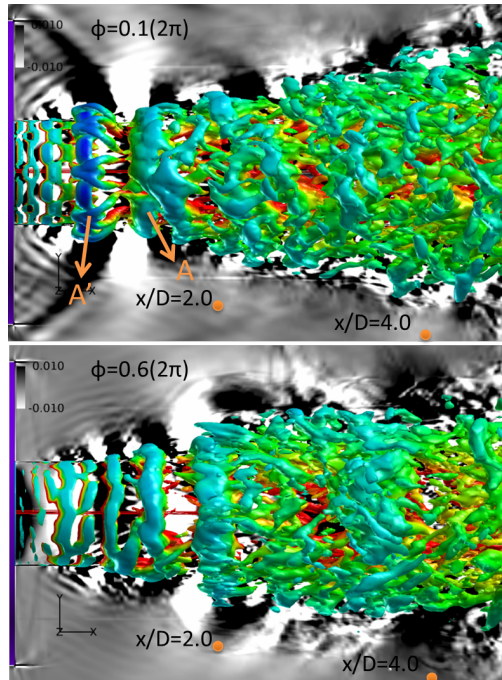


Figure 11: Iso-levels of Q-criterion colored by axial velocity with dilatation in gray scale for the $St=0.05$ cases

For the high frequency cases, rollers develop due to the excitation and these rollers grow and interact with other actuator induced structures as they propagate downstream. These rollers have been shown experimentally by Samimy⁷ and their nearfield interactions were documented by Sinha *et al.*¹⁷ The structures that are produced in phase $\phi = 0.6(2\pi)$ of Figs. 12 and 13 are the same as the impulse response structures in Fig. 11 but as the structures grow and propagate downstream they interact with the previously created actuated structure. The structures seen in Fig. 11 are labeled in Figs. 12 and 13 for comparison. Structures B and B' are equivalent to A and A' respectively and belong to the previous/subsequent actuator pulse. Figure 12 depicts the $St = 0.15$ cases in which the structures start to interact around an axial distance of $4D$. In phase $\phi = 0.1(2\pi)$, the characteristic structures seen in Fig. 11 are seen. Half a phase later A' is

broken up close to $x/D = 4$ while the ill formed B structure is colliding into the remains of A'. B' and B are similar structures to the ones denoted in the impulse case (Fig. 11) however structure B is not as well formed as structure A. While B' is more robust than the previous A' structure. This indicates a degree of feedback response of the structures between each excitation pair.

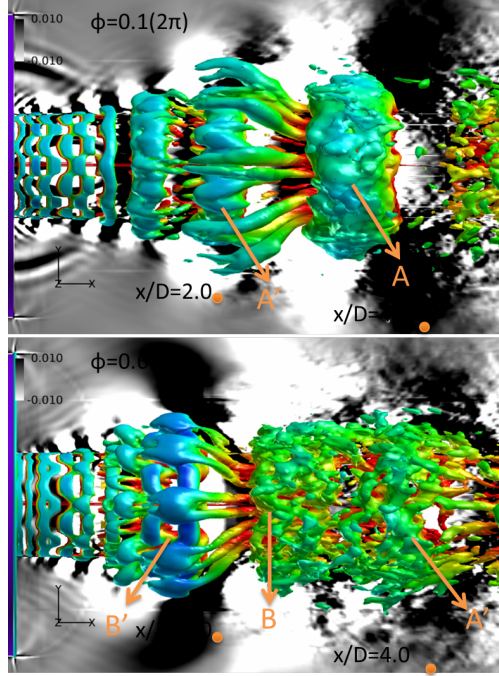


Figure 12: Iso-levels of Q-criterion colored by axial velocity with dilatation in gray scale for the $St=0.15$ cases

Figure 13 depicts the isolevels of the high frequency ($St = 0.25$) case in which the structures are interacting by an axial distance of $2D$. Since, the reaction to the actuation is cyclic the structures seen at the end of the potential core in one phase ($\phi = 0.1(2\pi)$) begin to develop in the other phase. Structure B/A' in phase $\phi = 0.1(2\pi)$ occurs when structure B collides into structure A'. This compression occurs due to the high convective velocity of B compared to A'. This interaction is quasi-linear creating a sine-like response in the near field pressure through linear superpositioning of the two actuator structures (B and A'). This quasi-linear superpositioning was also seen in Sinha *et al.*¹⁷ in the hydrodynamically dominant nearfield. This will be discussed further later in reference to Fig. 14.

The lipline phase-averaged pressure waveforms are now considered at $x/D = 3$ in Fig. 14a for each excitation frequency. The impulse response ($St = 0.05$) has a peak around the characteristic time of 5 and then a trough at $tU_{jet}/D = 6$. Note that a small secondary peak is seen after the trough which is not as distinguished in the experiments. This maybe due to the actuation model or the laminar nature of the nozzle exit. These peaks corresponds to the compressions and expansion from the coherent structures seen in Fig. 11 in which the structure is pushing fluid in front of it and behind it fluid is rushing in to fill the void the structure just left. This pressure field is similar to that of a uniform flow superimposed with a doublet. Note that the jitter outside this waveform is due to the low number of excitation periods averaged to obtain the phase-averaged waveform. If there were no computational constraints and this low frequency case was allowed to run for 100 excitation cycles the surrounding wiggles would disappear. The $St=0.15$ case is similar to the $St=0.05$ case however the time between excitation pulses is significantly reduced. For the $St=0.25$ case, the structures are interacting with each other significantly.

Figure 14b depicts the impulse response and $St=0.25$ phase-averaged waveform and the linearly superimposed impulse response waveform at a frequency of $St=0.25$ at an axial location of $3D$ on the lipline. This superposition of the impulse response consists of adding the impulse response to itself at a phase difference equal to that of the period of the $St=0.25$ case. The linear superposition on the lipline predicts the waveform shape and amplitude reasonably well. While the linear superposition does produce a secondary compression

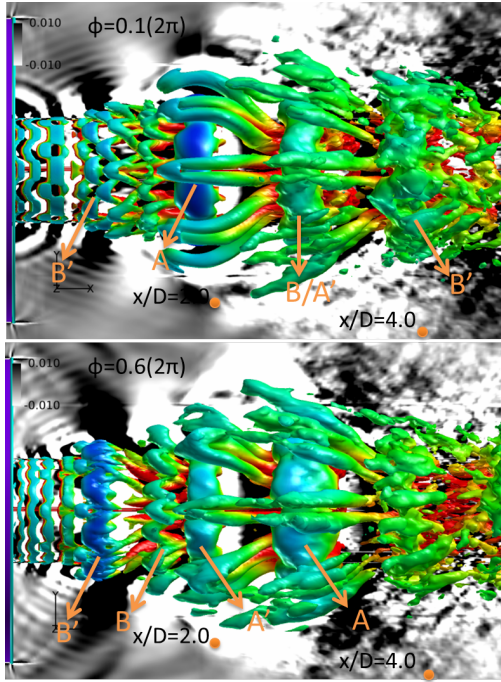


Figure 13: Iso-levels of Q-criterion colored by axial velocity with dilatation in gray scale for the St=0.25 cases

peak, it is far less prominent. Given the much greater amplitude of the pressure fluctuations along the jet lipline as compared to the irrotational near-field, it is perhaps unsurprising that nonlinear effects play a greater role. However, the interaction between the structures still appears to be governed predominantly by quasi-linear dynamics. This confirms the nearfield linear superposition findings of Refs.¹⁷ and³⁸ and extends it to the actual coherent structures.

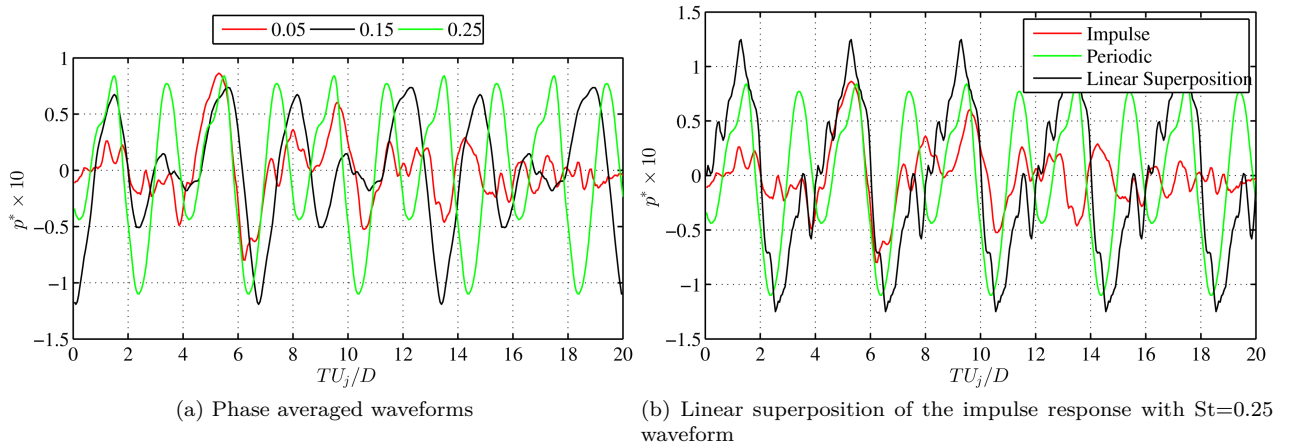


Figure 14: Lipline waveforms and superposed waveforms at $x/D = 3$, $r/D = 0.5$ for Mach 0.9

The development and decay of the structures can be further analyzed from correlations. Looking at the autocorrelations of the points along the lipline can confirm the visual findings of the coherence of the structures in Figs. 11-13. Therefore, Fig. 15 depicts the autocorrelations of pressure at $x/D = 2$ and 4 on the lipline. At $x/D = 2$, the subsequent correlation peaks located at every excitation period increase in amplitude with increasing excitation frequency. This higher temporal coherence maybe due to the decrease in number of actuation induced structures for a given time period for the lower excitation frequency cases.

Further downstream ($x/D = 4$), the subsequent correlation peaks are lower at all excitation frequencies than the upstream location indicating lower temporal coherence at this axial position. The bumpy appearance of the coherent structures (Figs. ??) implies that the structure is significantly changing each excitation period at this axial location.

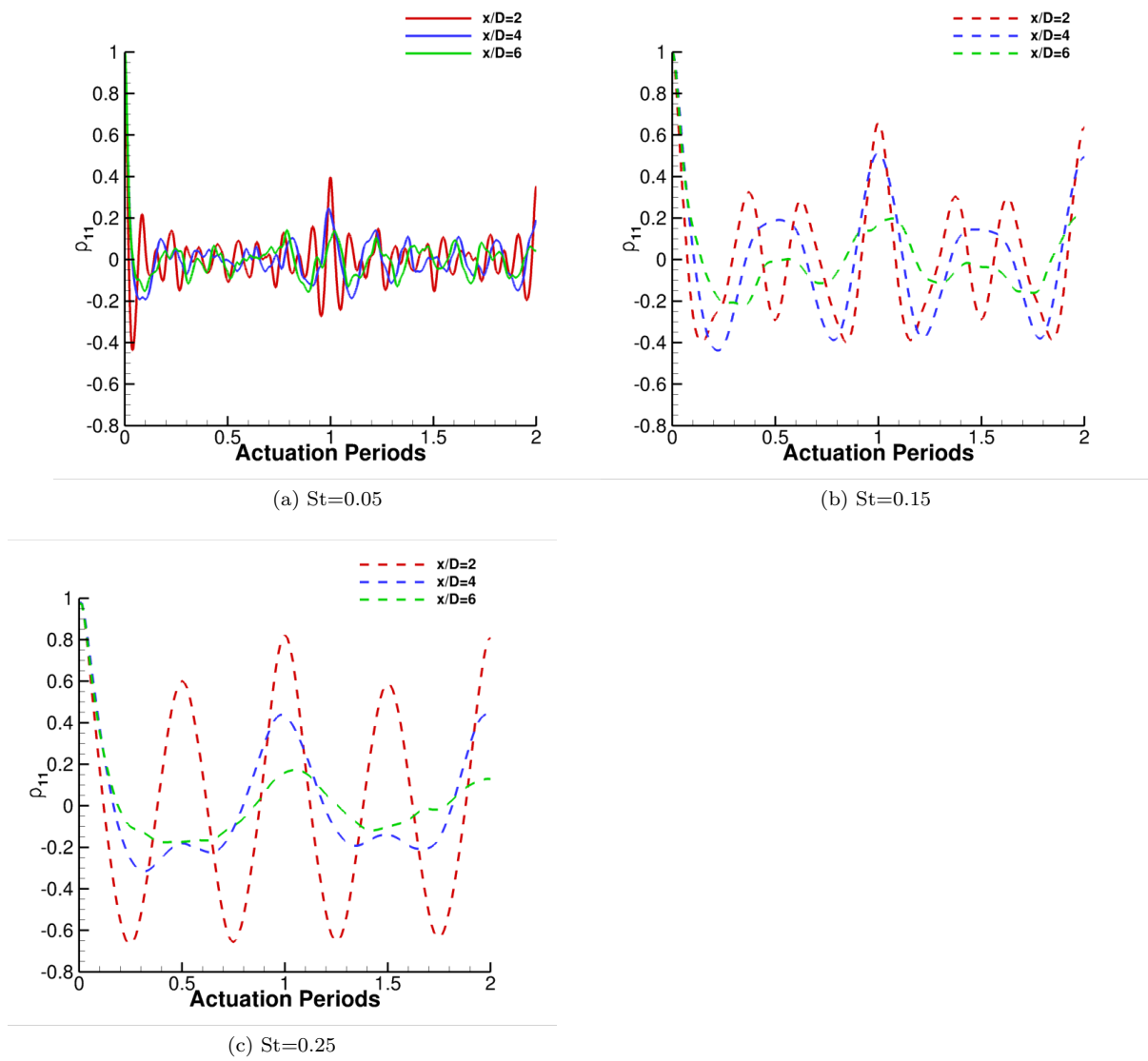


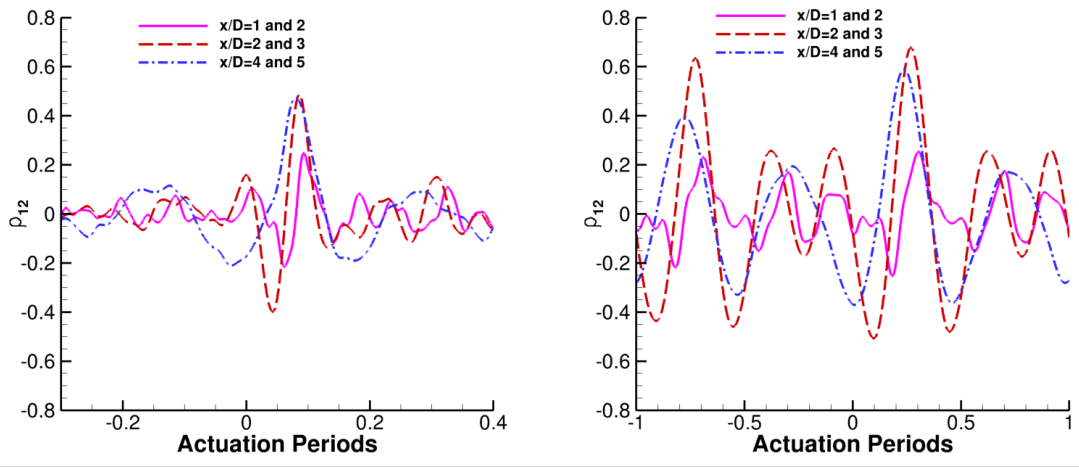
Figure 15: Auto-correlation of the lipline pressure

Figure 16 depicts the correlations between different points along the lipline to illustrate the convective velocity of the structures and the spatial coherence of the structures. The convective velocities of each case and axial position were computed from Fig. 16 and displayed in Table 1 for near the nozzle exit and for near the end of the potential core.

	No excitation	St=0.05	St=0.15	St=0.25
$x/D=1$ and 2	177 ($0.62U_{jet}$)	165 ($0.58U_{jet}$)	159 ($0.55U_{jet}$)	152 ($0.54U_{jet}$)
$x/D=2$ and 4	195 ($0.68U_{jet}$)	181 ($0.63U_{jet}$)	179 ($0.63U_{jet}$)	182 ($0.64U_{jet}$)

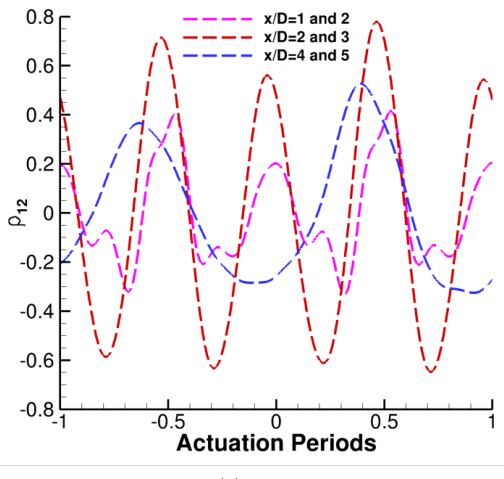
Table 1: Convective velocities from two-point correlations on the lipline

The jet is consistently increasing in convective velocity with axial distance for each case upstream of the end of the potential core. Therefore, the jet is entraining more core flow fluid near the nozzle exit which



(a) $St=0.05$

(b) $St=0.15$



(c) $St=0.25$

Figure 16: Two point correlations of the lipline pressure

increases the convective velocity. Further downstream, the ratios indicate that the entrainment is more evenly distributed between the high speed side and the low speed side.

III.B. Connecting the Large Scale Structures to the Hydrodynamic Near-field

The coherent structures presented previously in Section III.A cause disturbances in the near-field that can be seen in the near field pressure data. A more detailed analysis may be obtained through the study of

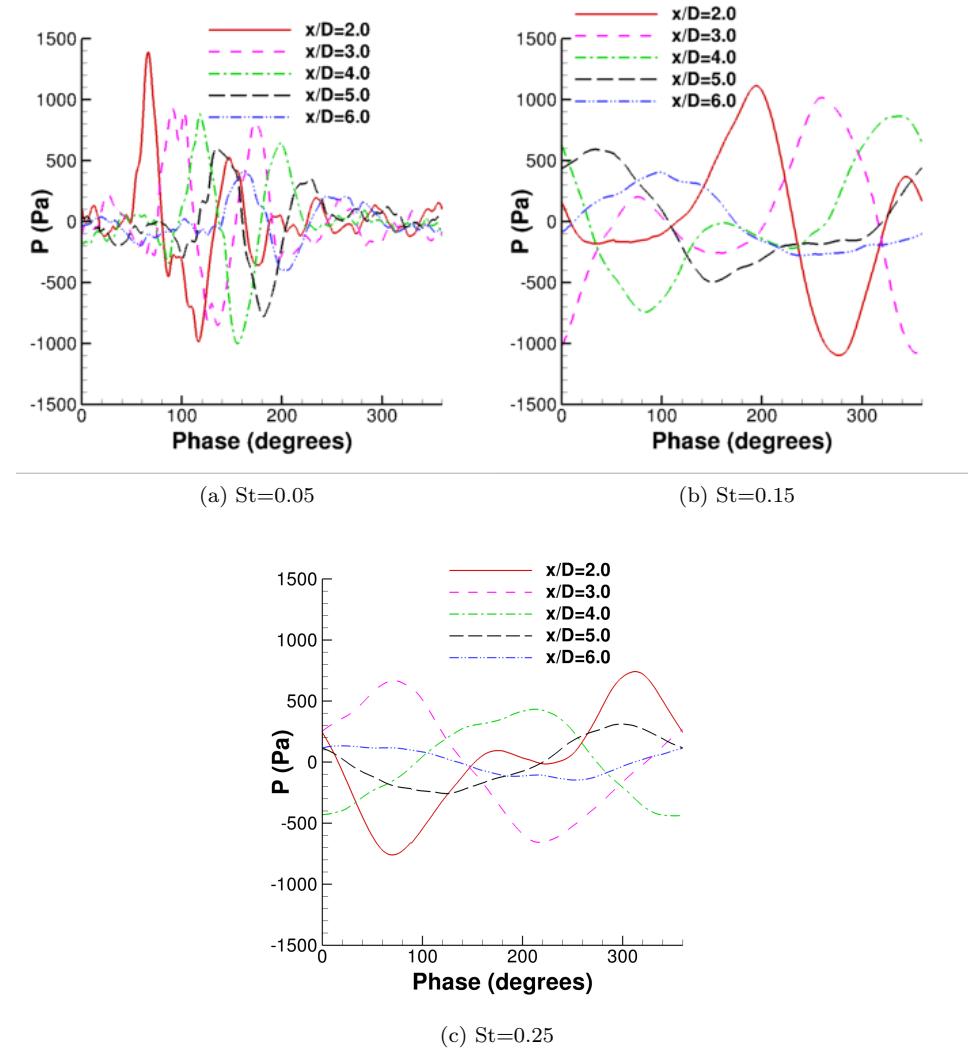


Figure 17: Phase-averaged pressure waveforms of *Array 1*

the phase-averaged signal close to the shear layer. Figure 17 depicts the phase-averaged point probe data along *Array 1* for the different excitation frequencies. The abscissa is the phase in degrees within the cycle. The waves dampen out with increasing axial distance which is due to the short potential core that causes the structures to reach their maximum potential early in the jet ($x/D = 2$). The propagation of the pulse is observed in the peaks which arise at successive locations with increased phase. The low frequency case ($St = 0.05$) depicts a long neutral period or "quiet" time between each pulse. After the core length ($x/D = 5$), the pulses are wider and no longer exhibit a sharp peak. As the excitation frequency increases and the actuator induced waves interact with each other more the amplitude of the waveforms decrease. This can be attributed to the linear superpositioning discussed for the lipline earlier (Section ??) and will be discussed further in regard to the nearfield later in this section. For each frequency, the phase-averaged waves are hydrodynamically dominated due to the proximity of the probes to the shear layer. However,

embedded in this signal is the acoustic response which will propagate to the farfield. This acoustic response can be separated from the hydrodynamic response through a wavelet method described and implemented in Ref.¹⁸ for a subsonic jet were there is a significant difference between the speed of the acoustic waves.

These nearfield phase-averaged waveforms can be connected to the coherent structures depicted in Figs. 11 to 13 and the pressure responses of the structures in Fig. 14a. The phase averaged structures of $St = 0.05$ in Fig. 11 depict a quiet time at an axial distance of $x/D = 2$ and 4 for the phase of $0.1(2\pi)$. This corresponds, at these locations, to the neutral period observed in Figs. 17a and b for a phase angle of 36° . With increase in phase, the structure moves to the right as observed in the succession of peaks in Figs. 17a and b. This corresponds to a convective velocity of $0.63U_{jet}$ between $x/D \sim 1$ and $x/D \sim 2$. This differs from the lipline convective velocities due to the increased influence of the acoustic waves outside the shear layer. This will be discussed more in terms of the two-point correlations. The large hydrodynamic wave at $x/D \sim 1$ at $0.1(2\pi)$ phase in Fig. 11 has just passed the axial distance of $x/D = 5$ (viewing range of the iso-level structures) at the $\phi = 0.6(2\pi)$ phase leaving the axial point in the top of the secondary compression peak. This corresponds to the smaller secondary peak at $x/D = 5$ at 216° in Figs. 17a and b.

For $St = 0.15$, the phase averaged signal at axial positions shown in Figs. 17c and d, indicates that the quiet time between pulses becomes shorter with downstream distance of the probe. This also corresponds with the increasing size of the structures in the jet. At an axial distance of $x/D = 4$, the horizontal neutral part of the phases is minimal, suggesting that the subsequent structure interaction is occurring. Correlating to Fig. 12 for the $St = 0.15$ case, the $x/D = 4$ location at $0.1(2\pi) = 36^\circ$ phase shows a large dilation wave associated with a well-developed roller. Clearly, the growth of the rings with distance from the nozzle exit corresponds to increasingly shorter quiet times at downstream probes: an effect clearly observed in Fig. 17c and d. Thus, at $0.1(2\pi)$ phase, $x/D = 2$ has significant quiet time while at $x/D = 6$ the pulses essentially merge with each other to create a sine-like response.

For the $St = 0.25$ supersonic case, the first axial position plotted has a sine-like wave indicating significant structure interactions. The subsonic case does not exhibit this sine-like state yet at this axial location due to the more prominent secondary compression wave that is seen in the impulse response at this location. The waves maintain a sine-like pattern beyond $x/D = 2$ even after the potential core ($x/D = 5.5$).

Figure 13 can be used to give a visual understanding of these phase-averaged pressure probes for the $St=0.25$ cases. In Fig. 13, the white dilatation waves correspond to an increase in pressure while the black dilatation waves correspond to a decrease in pressure. At a phase of $\phi = 0.1(2\pi) = 36^\circ$ in Fig. 13a, the $x/D = 4$ point probe is entering a white dilatation region (increase of pressure) while the $x/D = 2$ probe is entering a black dilatation wave corresponding to a decrease in pressure. In Fig. 17a, an increase of pressure is seen at $x/D = 4$ and a decrease is seen at $x/D = 2$ for the phase of 36° . At a phase of $\phi = 0.6(2\pi) = 216^\circ$, the $x/D = 2$ location is in the region of pulse interactions where structure B and A' are beginning to merge. This area translates to a bumpy uphill region for $x/D = 2$ in Fig. 17c. After the two structures (A' and B) merge ($\phi = 0.1(2\pi)$) around an axial distance of $3D$, the phase averaged point probe depicts a wiggle in the increasing pressure.

Figure 18 depicts the auto-correlations of pressure for the first array for each excitation case. The peak correlations decrease with axial distance as more fluid is entrained modifying subsequent structures in different ways and the jet becomes more turbulent. The axial positions beyond the potential core show the greatest reduction in correlation. This enhanced decay in correlation is also seen in the experimental results at Mach 0.9 (Alkandry *et al.*⁴¹). This indicates that the hydrodynamically dominated nearfield of the subsonic jet has low temporal coherence, which implies that the waves passing through these points are changing significantly from excitation period to excitation period. This change could be due to a combination of effects including: the entrainment seen by the jet which would alter each structure differently and the higher natural turbulence with axial distance.

Figure 18a depicts the low excitation frequency autocorrelations. For the points within the potential core, the correlation value quickly drops below zero with increasing lag until a phase of $0.1(2\pi)$. Beyond this phase, the axial positions of $2D$ and $4D$ maintain significant correlation values except for the range in between each period of $0.4(2\pi)$ and $0.6(2\pi)$. In general for all excitation frequencies, the integral time scale increases with axial distance as the structures in the shear layer become larger or resultant waves from the coherent structures on the lipline decrease their convective velocity. Beyond the potential core, the hydrodynamically dominated waves are moving at a slower speed than in the potential core region. The convective velocities will be discussed further in regards to the two-point correlations.

The $St = 0.15$ case (Fig. 18b) depicts a secondary smaller hump located in between each excitation

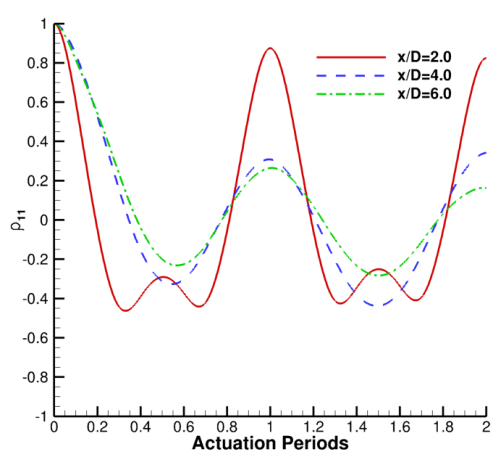
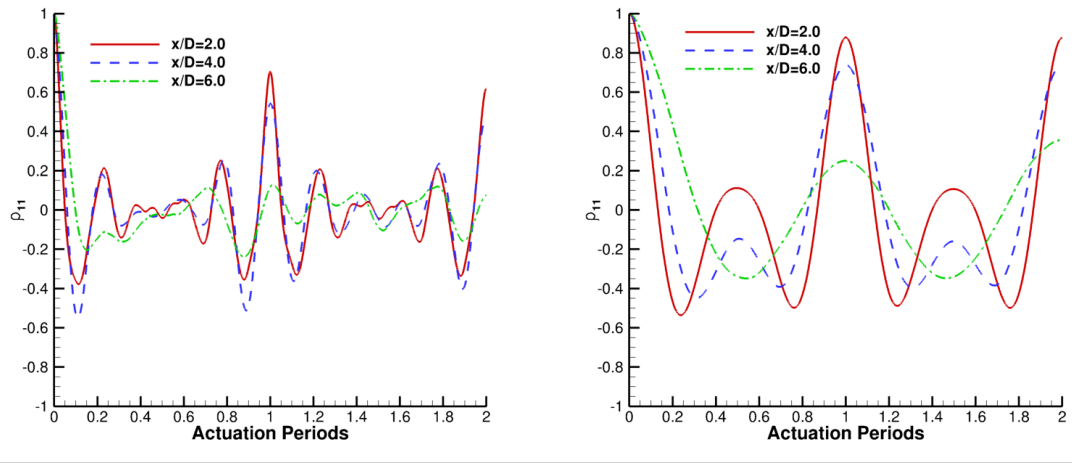


Figure 18: Auto-correlation of the near field pressure for the first array

period for the points within the potential core. This rise between periods is similar to removing most of the zero correlation region between the actuation periods in the impulse response autocorrelations and signifies the beginnings of subsequent structure interactions. Beyond the potential core at an $x/D = 6.0$ a trough is present.

The high frequency cases in Fig. 18c, exhibit a sine-pattern inside the potential core region ($x \leq 5.5D$) with peaks at intervals corresponding to the excitation frequency except for the $x/D = 2$ location. This location has a hump at the half period indicating the beginning of structure interaction. After the potential core, the correlation values decay slowly to zero throughout time. A decrease in subsequent period peaks is seen with axial distance. This decrease in peak correlation values with axial distance is due to the decrease in organization of large scale structures beyond the potential core and thereby organization of the surrounding nearfield.

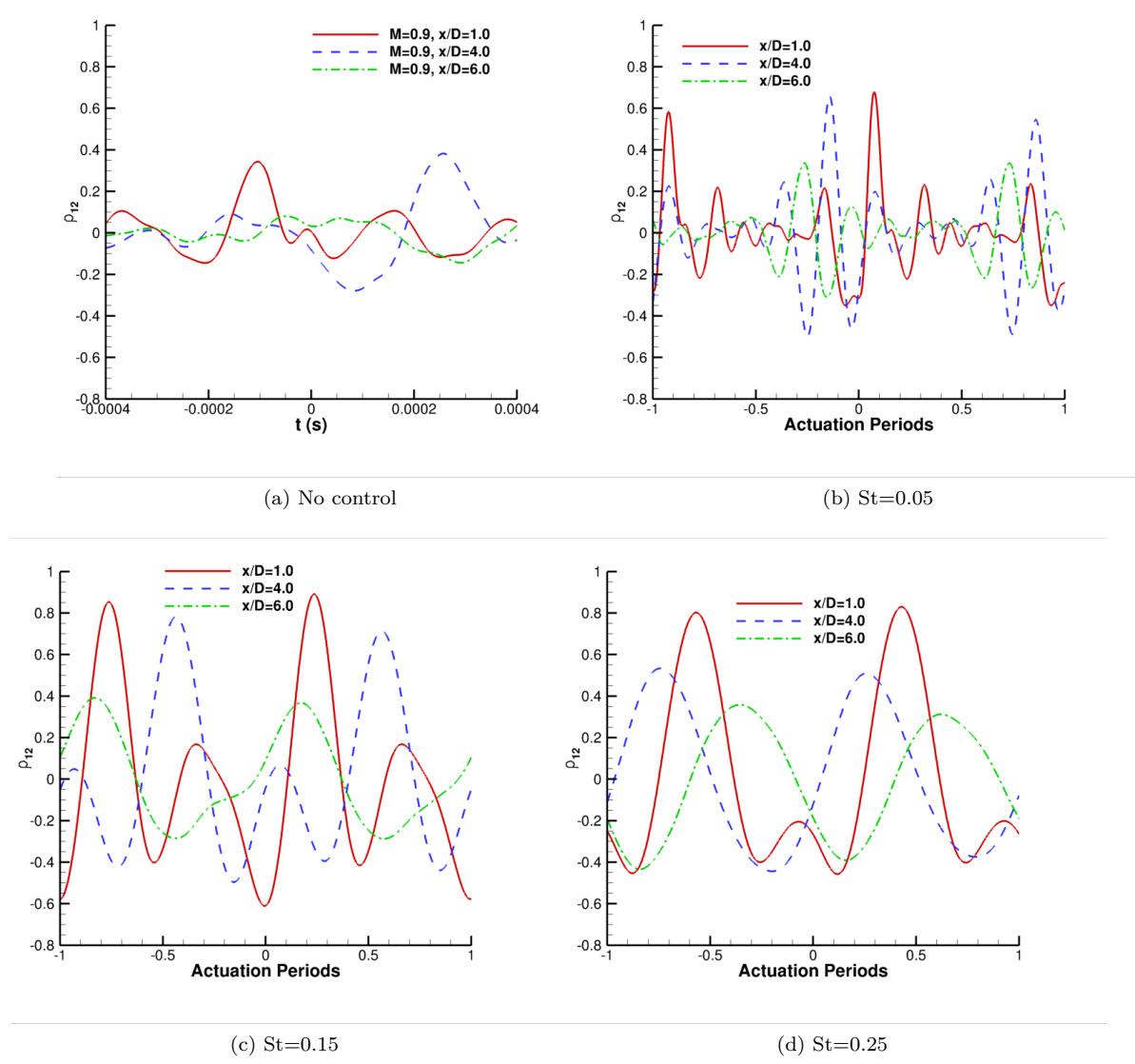


Figure 19: Two-point correlation of the near field pressure for the first array with $x/D=2$ and $r/D=1.355$

Figure 19 portrays the two-point correlations of pressure comparing the first array point probes to the $x/D = 2$ location on the first array. For the impulse response case (Fig. 19a), the correlations decay rapidly with axial distance. This shows that not only that there is low temporal coherence (see Fig. 18) but also that there is low spatial coherence; meaning the structure changes significantly as it propagates downstream. The $St = 0.15$ case (Fig. 19b) exhibits a more sine like pattern with the characteristic hump seen in the autocorrelations which likewise indicates structures beginning to interact in the shear layer. For

a phase difference of $0.5(2\pi)$ in the $St = 0.15$ cases, a high correlation value is seen for the $4D$ axial location. Connecting this correlation to the coherent structures in Fig. 12 there is a dark dilatation wave (decrease in pressure) at the $4D$ location for the phase of $0.1(2\pi)$ and half a phase later, $0.6(2\pi)$, the $2D$ point is located in a dark dilatation region indicating a high correlation between these two points every half excitation period.

The two-point correlations for the high frequency case (Fig. 19c) exhibit a sinusoidal response except for the first axial position shown ($x/D = 1$). For an axial distance of $1D$, a high positive correlation is obtained half an excitation period away. Therefore, in Fig. 13a, when $x/D = 2$ is encountering a white dilatation wave (increase in pressure) at a phase of $\phi = 0.1(2\pi)$, $x/D = 1$ will experience a white dilatation wave also half a period later ($\phi = 0.6(2\pi)$). Similarly, a negative correlation value is observed for $x/D = 1$ at a phase difference close to zero. Therefore, in Fig. 13a for a phase of $\phi = 0.6(2\pi)$, the axial position of $1D$ has a black dilatation wave instead of the white dilatation wave that $x/D = 2$ has for the same phase. As the structures break apart at the end of the potential core, these relationships also degrade. The peaks closest to zero in the two-point correlations have the highest maximums. Therefore, each structure will be more correlated to itself further downstream than to the previous/subsequent structures. This can be attributed to the random perturbations in the jet that adjust each actuated structure differently.

	No excitation	$St=0.05$	$St=0.15$	$St=0.25$
$x/D=1$ and 2	$243 (0.85U_{jet})$	$188 (0.66U_{jet})$	$180 (0.63U_{jet})$	$165 (0.59U_{jet})$
$x/D=2$ and 4	$197 (0.69U_{jet})$	$202 (0.71U_{jet})$	$197 (0.69U_{jet})$	$192 (0.67U_{jet})$

Table 2: Convective velocities from two-point correlations on Array 1

The velocity of the waveforms surrounding the jet can be computed from the correlations of Fig. 19 for the near field probes on Array 1 two investigate the change in convective velocity from the lipline (shown in Tables 1) to the hydrodynamically dominated nearfield. Table 2 lists the average velocity of the waves between the axial point of $1D$ and $2D$ on Array 1 and the velocities of the waveforms that travel between $x/D=2$ and 4 . These velocities are consistently higher than the convective velocities observed in Section III.A on the lipline but display similar trends. The hydrodynamic waves will decrease exponentially with radial distance away from the shear layer leaving the near field dominated by waves traveling at the speed of sound. Therefore, the velocities in the nearfield are higher than the convected structures in the shear layer due to the increasing influence of the acoustic waves. This is important to take into account for experimentalists who compute the convective velocity of the structures from the nearfield due to limitations in temporal resolution of PIV of the actual shear layer.

III.C. Forced Structures and Natural Structures

During their way downstream of a jet, forced large turbulent-structures are producing pressure wave-like form that can be sensed by the near-field pressure line array (microphones or numerical probes): this is the 'signature' left behind their passage. The signatures of those forced large turbulent-structures can be appreciated on figure 17 for three different excitations, $St \in \{0.05, 0.15, 0.25\}$. These were obtained using a phase-average technique. The signature for the case $St = 0.05$ present a distinct time-scale while the higher excitation signatures, $St \in \{0.15, 0.25\}$, does not and are quasi-sinusoidal. This is due to the increasing interaction between successive structures for these excitations.

It is not possible to use the phase-average with the unforced case as the phase-average is using the actuation times as the phase to do the average on. It is necessary to use an alternative averaging method in order to appreciate a similar signature due to unforced jet turbulent-structures. Instead of the phase-average, a wavelet-based method, namely the wavelet-conditioning, was applied to the unforced and forced cases.

III.C.1. Wavelet conditioning

The wavelet-conditioning was used for structure identification in jets and other turbulent flows.⁴²⁻⁴⁶ The technique is based on the use of the so-called Local Intermittency Measure or LIM, introduced in 1992 by Farge *et al.*⁴⁷ The LIM is the ratio between two energies: a local energy for a specific time and scale (τ, s) and an averaged energy in time for the same scale s . The LIM was demonstrated to be a well suited indicator for coherent structures identification.⁴² Its mathematical expression is:

$$L(s, \tau) = \frac{w^2(s, \tau)}{\langle w^2(s, \tau) \rangle_\tau} \quad (2)$$

where $w^2(s, \tau)$ is the local energy for a specific time and scale, and $\langle \bullet \rangle_\tau$ represents a time average. As a ratio between positive quantities, LIM can only be positive ($L \geq 0$). LIM gives an information about the fluctuation of energy and by choosing a proper threshold T it is possible to select a set of times $\{\tau_i\}$ corresponding to peaks with value greater than the threshold T . The peaks are local maxima of LIM and are respecting the following conditions:

$$\left\{ \begin{array}{l} L(s, \tau) > T, \\ \frac{\partial L}{\partial \tau}(s, \tau) = 0, \\ \frac{\partial^2 L}{\partial \tau^2}(s, \tau) < 0, \end{array} \right. \quad (3)$$

An iterative process was used in order to fixe the threshold T . To initiate the iterative process it is needed first to select a 'first estimate' of the threshold. It was taken to be equal to 1. The algorithm of the iterative process is applied to each scale of the wavelet-decomposition and allows to have a threshold for each scale. The algorithm used to obtain this:

1. Select a first threshold to initiate the iterative process (1 in the present case)

2. Evaluate the coefficient

$$R(T) = -\frac{\log\left(\frac{N_p}{N_m}\right)}{\log\left(\frac{\sigma_{w_p}}{\sigma_{w_m}}\right)} \quad (4)$$

where N_p is the length of the set $\{L > T\}$, N_m is the length of the set $\{L \leq T\}$, σ_{w_p} the standard deviation of the set $\{w(\tau_p) | L(\tau_p) > T\}$ and σ_{w_m} the standard deviation of the set $\{w(\tau_m) | L(\tau_m) \leq T\}$

3. Re-evaluate T

4. Iterate points 2 and 3 until T achieve the maximum of L for the scale under analysis

The outcome of the iterative process is a vectors: one containing the different value of T and the second the different value of $R(T)$. The threshold for the analysis is the selected as the one corresponding to the maximum of $R(T)$.

The next step is to get similar results to those obtained with the phase-average. In order to get the signatures, a conditional-average (eqn. 5) using the set of times $\{\tau_i\}$ is performed. In some way, the conditional-average and phase-average are similar: the set of times $\{\tau_i\}$ replaces the phases on which the phase-average is performed. At each time location corresponding to a peak of energy, a window W of fixed time-length l_W is selected from the original signal $p(t)$. The conditional-average, \tilde{p} is calculated from this set of windows:

$$\tilde{p}_m^n(W) = \langle p_m | P_k \rangle_{\tilde{\tau}_s^n} = \frac{1}{N^n} \sum_{i=1}^{N^n} p_m(\xi_i), \quad (5)$$

where the superscript n and subscript m stand for the position of the reference signal and of any other signal of the array, respectively, the subscript s stands for the scale, N^n is the number of detected events, $\tilde{\tau}_s^n$ is the set of corresponding times for a specific scale s at which these events are occurring and $\{\xi_i\}$ is the interval surrounding each peak, $\xi_i \in [\tilde{t}_i - \frac{l_W}{2}, \tilde{t}_i + \frac{l_W}{2}]$, $\tilde{t}_i \in \tilde{\tau}_s^n$. A first analysis using equation 5 was performed on the microphones line-array. A second analysis was then performed by doing the conditional-average only with peaks with negative/positive value in the real domain (pressure). Figure 20 presents the two subfigures for the different cases (negative/positive peaks) and a third subfigure to compare them:

- (a) conditional-average (eqn. 5) using only the negative peaks
- (b) only the positive peaks
- a comparison between the two previous one ((a) was inverted in order to compare it to (b))

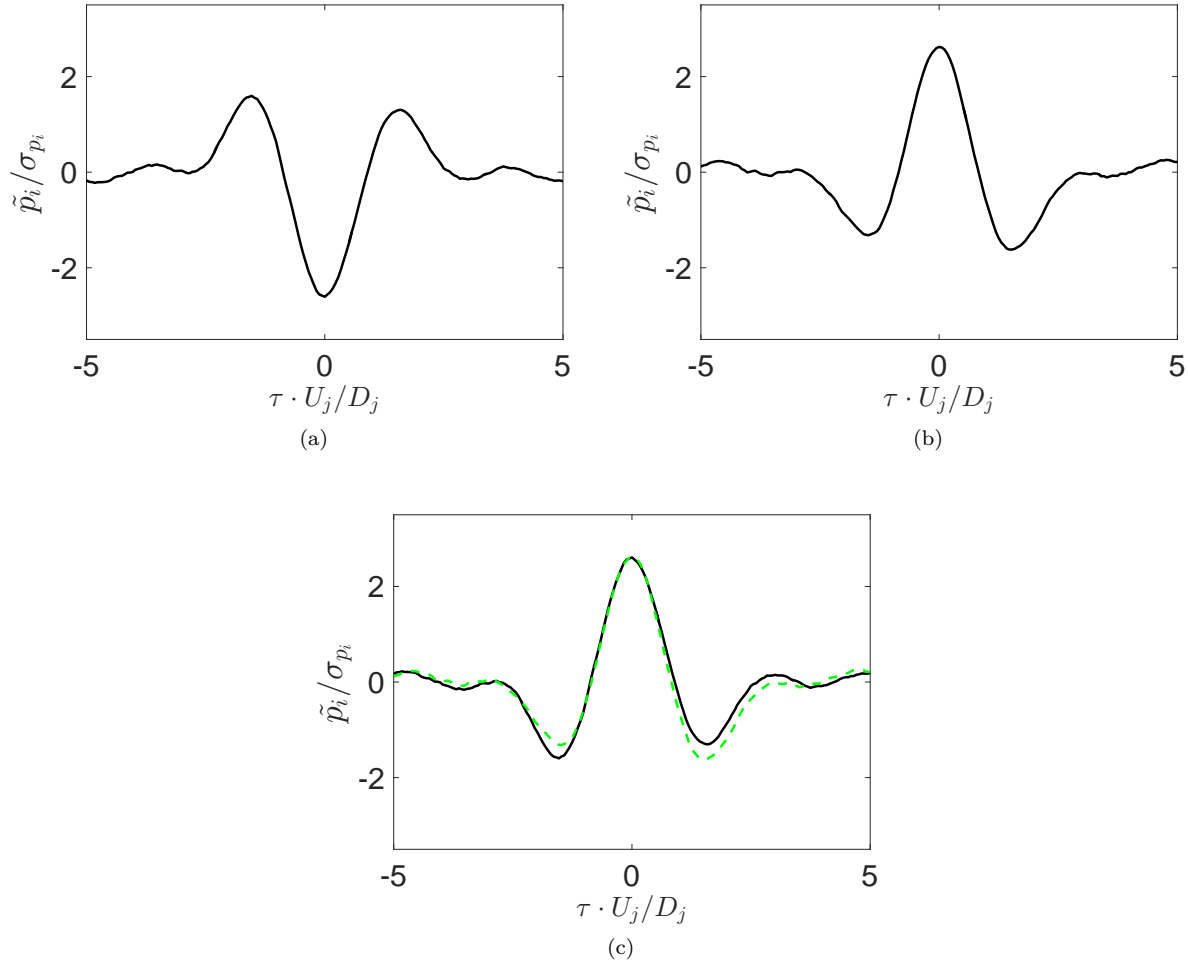


Figure 20: Auto-conditioning signatures of the signal at $x/D = 3$, (a) with only negative peaks, (b) with only positive peaks, (c) comparison between the signatures

Subfigure (c) of figure 20 presents the resemblance between the signature of subfigures (a) and (b) on which the conditional-average was performed using only negative or positive peaks (it is important to understand that the differentiation is done by evaluating the value of each peak in the real domain and not in the LIM/wavelet domain). At this point, it is believed to be the result of the passage of two successive large scale turbulent-structures, in the zone where their interaction take place. The formulation of the conditional-average was modified to take this observation into account and reformulated as follow:

$$\tilde{p}_m^n(W) = \langle p_m | P_k \rangle_{\tilde{\tau}_s^n} = \frac{1}{N^n} \sum_{i=1}^{N^n} \text{sign}(p_n(\tilde{t}_i)) p_m(\xi_i), \quad (6)$$

$\text{sign}(p_n(\tilde{t}_i))$ is introduced to take into account the sign of the peak in the real domain. This operation might be unnecessary for an experimental database (of long time-series) but for a numerical database which is strongly limited in its time duration it improve the results obtained with the wavelet-conditioning. The conditional-average using eqn. 5 with all the peaks in not presented here as not relevant as an additional proof for the separation between negative/positive peaks. When the conditional-average is performed on a signal p_n by using its own set of times $\tilde{\tau}_s^n$, and so $n = m$: this is the auto-conditioning. If the conditional-average of a signal p_m is done by using the set of times of a signal p_n , and so $n \neq m$: it is then called cross-conditioning. The auto/cross-conditioning are presented on figure 21: the top is the auto-conditioning where the selection of W is done in the reference signal n ; and the bottom is the cross-conditioning of another signal m where W is centered around the times obtained with signal n .

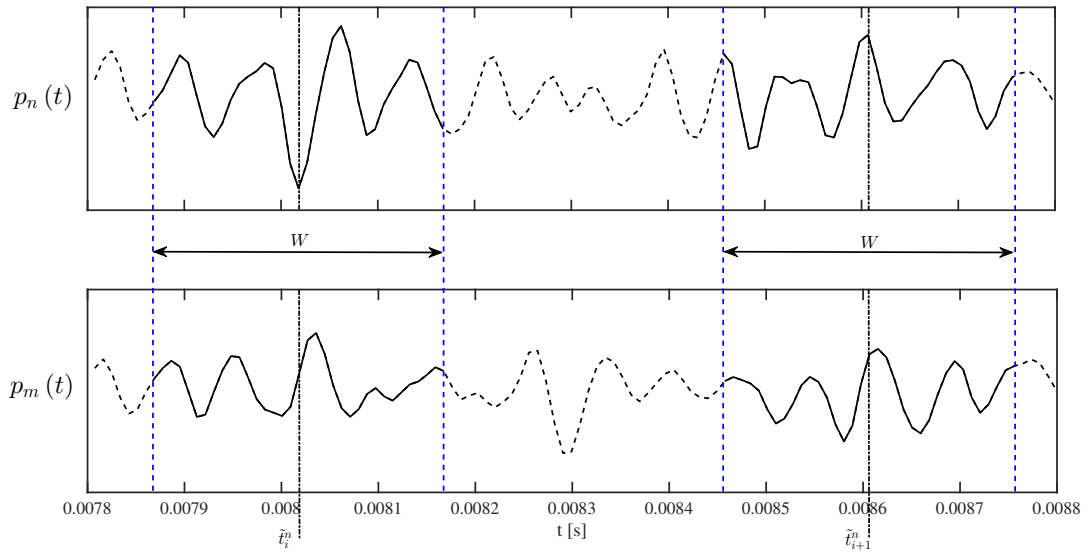


Figure 21: Auto-conditioning of a signal $p_n(t)$ and cross-conditioning of a signal $p_n(t)$

For more information about the wavelet-transform, see.⁴⁷

III.C.2. Turbulent-structures identification

The wavelet-conditioning was used on the experimental and numerical databases. Four cases are presented here ($S_t \in \{0, 0.05, 0.15, 0.25\}$). The wavelet-conditioning was first applied to the experimental database as it is sure to achieve convergence: the signals are sufficiently long to have enough events selected in order to achieve convergence with the conditional-average 6. It is easier then to know what to expect from the numerical database. The figures presenting the wavelet-conditioning for the experimental and numerical databases were split in two: two figures for each database. Each figure contains two cases: figures 22 and 24 contain the unforced and forced at $S_t = 0.05$ cases and figures 22 and 24 contain the forced at $S_t \in \{0.15, 0.25\}$. The curves with a central peak on each subplot are corresponding to the auto-conditioning: the selection of peaks and the conditional-average were done on the same signal (here the signal at $x/D = 3$). The other curves on each subplot are corresponding to cross-conditioning: only the conditional-average was

performed on these signals using the set of times $\{\tau_i\}$ obtained with the signal at the previous mentioned axial position. Figures 22 and 23 here after were obtained with the experimental database. The first observation is that the wavelet-conditioning is able to achieve similar results as the phase-average. The unforced case (a) and forced case at $S_t = 0.05$ (b) present a signature on which it is possible to read a time-scale. The shape of both is different though and might be the result of energy provided to the flow by the actuators. The forced cases at higher Strouhal number dont present a similar signature and instead have a quasi-sinusoidal behaviour. It was expected from the phase-average results of figure 17.

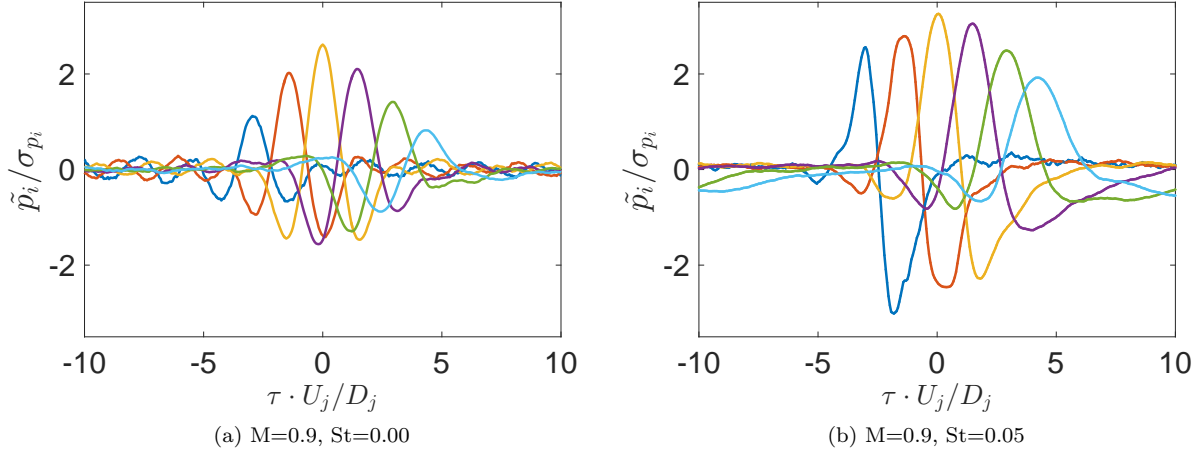


Figure 22: Wavelet-conditioning of the experimental database, *Array 1*, $S_t \in \{0.00, 0.05\}$

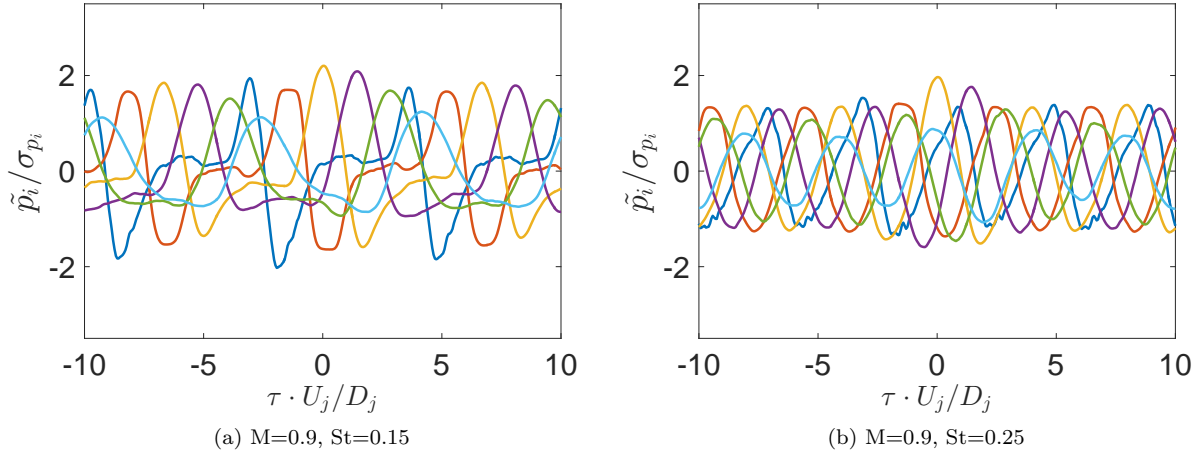


Figure 23: Wavelet-conditioning of the experimental database, *Array 1*, $S_t \in \{0.15, 0.25\}$

Figures 24 and 25 were obtained with the numerical database. As expected from the previous results, the unforced case and forced case at $S_t = 0.05$ from figure 24 present a signature with a explicit time-scale. The higher Strouhal number are again presenting a quasi-sinusoidal behaviour.

It is important to remind that the time length of each database is different and have its influence on the results: while the conditional-average is done on several hundreds/thousands events for the experimental database, it is done on less than a hundred of events for the numerical database. This is the main reason for the noisier results of the numerical database. The other reason might come from the numerical model of the LAFPAs: while it preserves the main features of the actuators it might not inject as much energy as the experimental LAFPA to the flow.

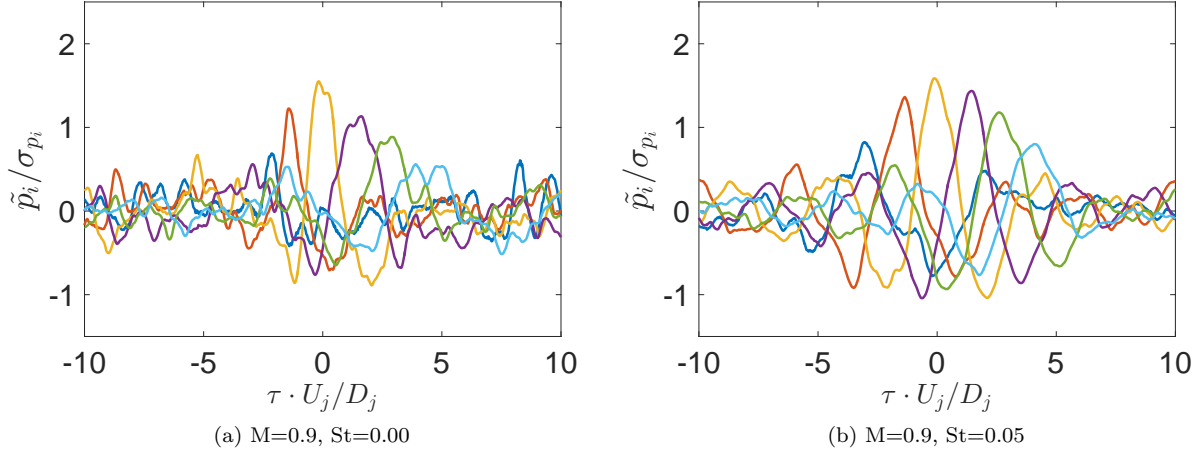


Figure 24: Wavelet-conditioning of the numerical database, *Array 1*, $S_t \in \{0.00, 0.05\}$

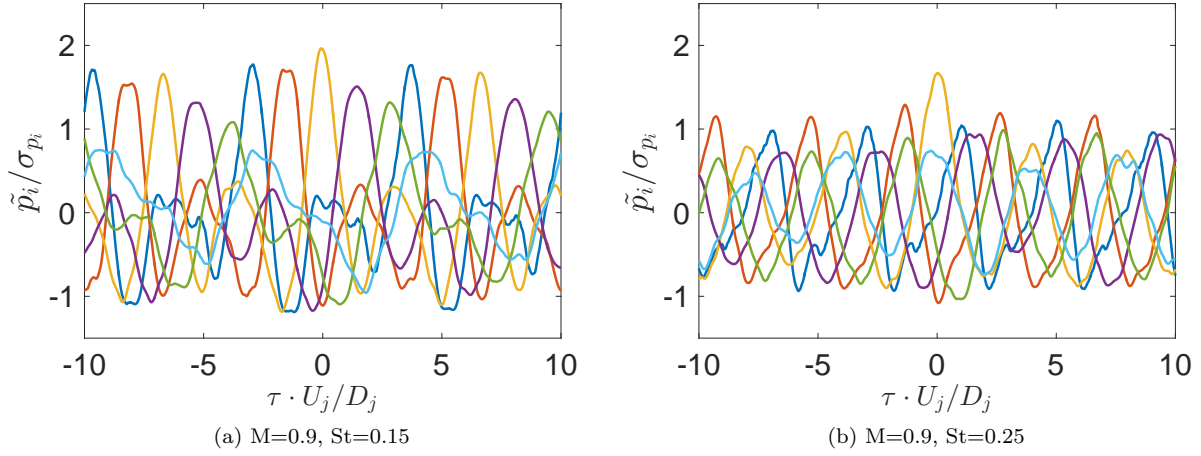


Figure 25: Wavelet-conditioning of the numerical database, *Array 1*, $S_t \in \{0.15, 0.25\}$

The numerical database was limited to the four cases presented here but the experimental database is containing 3 more cases: $S_t \in \{0.020, 0.350, 0.50\}$. Jet excited at lower Strouhal number $S_t \leq 0.05$ presents a similar behaviour as the one described above with a explicit time-scale and greater Strouhal number does not.

III.C.3. Acoustic and Hydrodynamic Decomposition of the Nearfield

Due to this complicated combination of the acoustic and hydrodynamic waves in the near shear layer region, the first array is decomposed into hydrodynamic and acoustic signals using the method presented in Crawley *et al.*³⁸

III.D. Linking The Large Scale Structures to the Acoustic Nearfield

The phase-averaged waveforms in the $M=0.9$ cases generated by the excitation are explored again, this time at the furthest spatially resolved axial and radial position simulated (which corresponds to $x/D = 20.0$, $y/D = 9.0$), as shown in Fig. 26. Like the hydrodynamically-dominated waveforms shown in Fig. 14, excitation of the jet at a very low Strouhal number produces a compact, impulsive disturbance in the near

acoustic field. And, as before, increasing the excitation frequency results in a periodic wave, which can be constructed by a linear superposition of the impulse response. The validity of the linear superposition model (Fig. 26b) breaks down more quickly than the lipline results. While the periodic response at $St = 0.15$ can be approximated with the impulse response (Fig. 26b), the periodic response at $St = 0.25$ cannot (not shown) for this point in the nearfield. This maybe due to the complex interactions of the waves in the nonlinear region of the jet that alters the acoustic response while maintaining the form of the large scale coherent structures on the lipline.

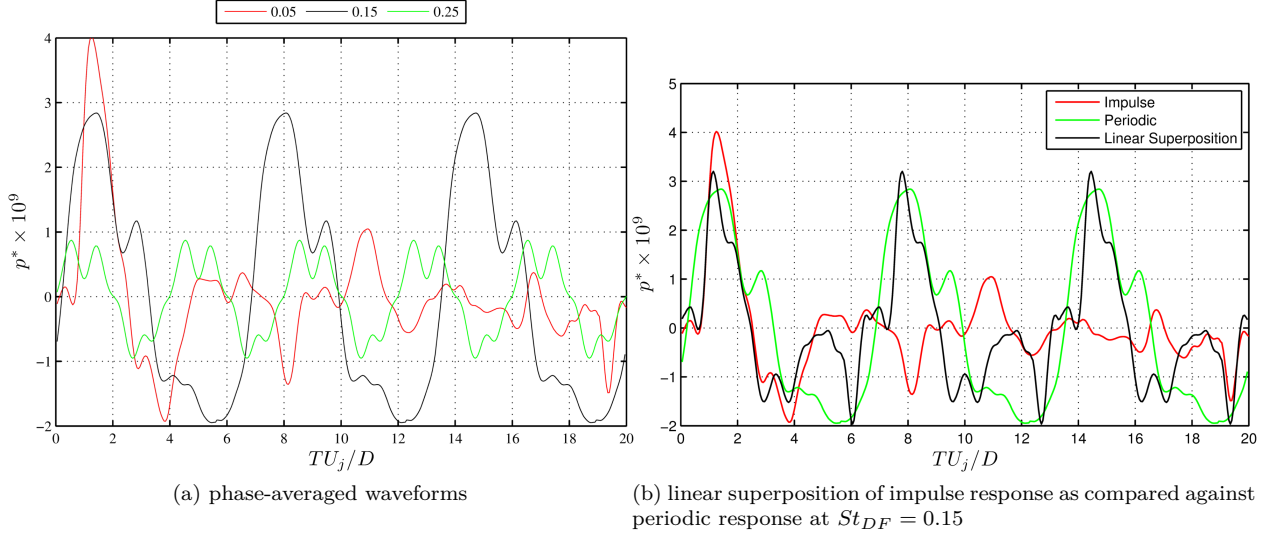


Figure 26: Response to excitation in the nearfield at $x/D = 20.0, y/D = 9.0$

To further understand the dynamics of this acoustically dominated region, two-point correlations between Array 1 in the near-field and the furthest spatially resolved axial and radial position ($x/D=20.0, y/D=9.0$) were analyzed in order to locate the dominant acoustic source region. The lags (y-axis) are normalized by the ambient speed of sound (a_∞) and the distance (R) that each point on the array is away from the far radial point ($x/D=20.0, y/D=9.0$). The results exhibit correlation regions which match quite well with the convective velocity of the large scale structures (values correspond to those in Table ?? and are plotted as τ_{con}), especially in the region of the potential core where the large scale structures are more coherent. Due to the normalization of the abscissa, the time that it takes an acoustic wave to reach the far radial point is $\tau a_\infty / R = 1$ and is labeled as τ_{ac} . The portion of the array that is downstream of the collapse of the potential core exhibits waves that are traveling at acoustic speed for all cases. This is less evident in the no-control case due to the lower coherence exhibited in the correlations compared to the excitation cases. In the downstream region, the positive correlation diverges from this on-axis acoustic propagation and instead follows a curve indicative of off-axis acoustic propagation. This curve is indicative of the time delay seen by the first Array if a source emits a wave on the centerline of the jet and propagates to the far radial point. This line is marked as τ_s in Fig. 27. For the natural jet, the slope of the divergence indicates an acoustic source region extending downstream to about $x/D = 7.5$ on the centerline. For the controlled cases, the source region is extends to an axial position of $6D$.

The overall directivity and potential noise source region can also be seen from correlation plots of the entire nearfield to one far radial point. Figure 28 depicts the maximum correlation value of each point on a streamwise slice of the jet to the 30° nearfield angle for each case. There is a clear directivity of the correlations toward the jet core until $x/D=4.5$. The correlation contours have an angle of about 32 degrees for both subsonic and supersonic cases. The nearfield correlated region becomes narrower with increasing excitation frequency due to the large actuation induced structures dominating the flow which consistently break up in the same axial locations.

III.E. Connecting the Near-field to the Far-field

Decomposition of the near-field into its constitutive acoustic and hydrodynamic components is desired, in order to simply analysis of the responses of the individual fields. The strong hydrodynamic pressure

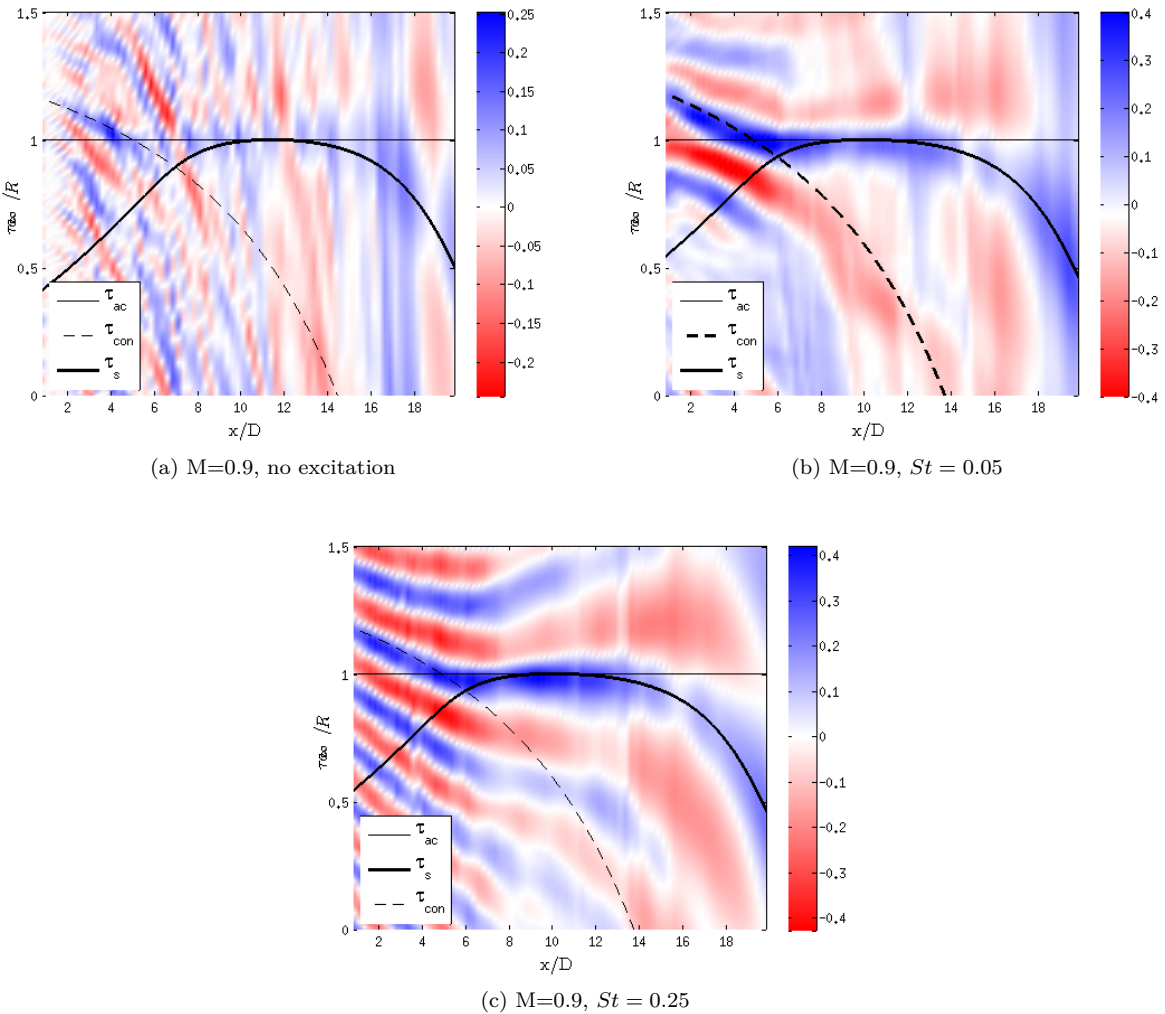


Figure 27: Two-point correlations of computational results between the full near-field to the furthest downstream and radial position ($x/D = 20$, $r/D = 9$)

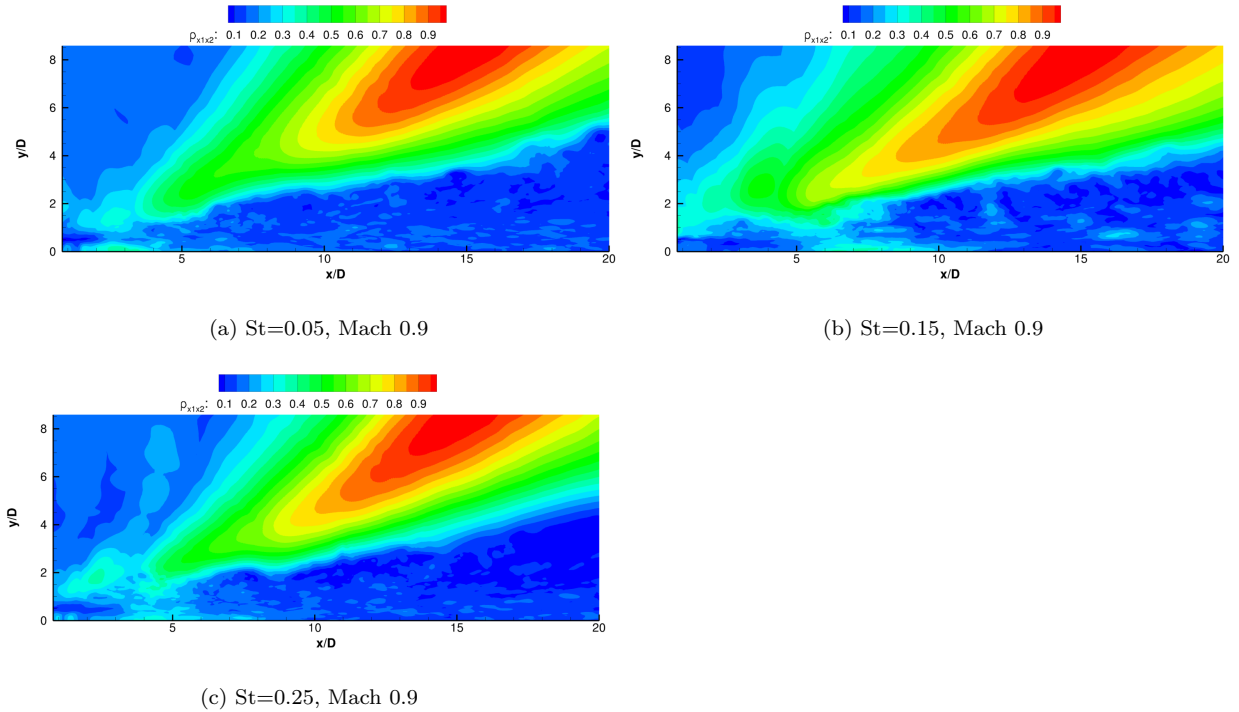


Figure 28: Maximum correlation of the near field pressure with the 30 degree polar angle

fluctuations associated directly with the passage of coherent structures largely mask the resultant weak acoustic signal. As has been shown by Arndt *et al.*,⁴⁸ the irrotational near field of the jet comprises both the hydrodynamic footprint of the large-scale structures in the mixing layer as well as acoustic radiation. The analysis of Coiffect *et al.*⁴⁹ showed that the total near field can be thought of as a linear superposition of the hydrodynamic and acoustic fields. Therefore, a suitably designed linear filter can, in principle, extract the constitutive fields from the experimentally measured near field.

This was first done experimentally by Tinney & Jordan,⁵⁰ using a linear array of microphones and a wavenumber-frequency filter in the Fourier domain to separate the irrotational near-field into subsonically- and supersonically-conveying waves. In the current work a similar method is used, though the two-dimensional Fourier transform has been replaced with a spatio-temporal wavelet transform. Details of the decomposition algorithm and validation in the experimental results can be found in Crawley & Samimy.⁵¹

III.E.1. Far-Field Response

The quasi-linear interaction model which was found to govern the response of the jet to excitation in the flow-field and the irrotational near-field was in fact also found to hold for the acoustic far-field as well, at least at aft angles (where the acoustic signal is strongest and is known to correlate well with large-scale structures). This can be observed in Fig. 29a, where the phase-averaged response of the jet has been plotted for the far-field signal at a polar angle of 30°. For legibility, only a select number of excitation Strouhal numbers from the experimental jet have been included. As with the hydrodynamic pressure field, the acoustic far field exhibits a compact waveform for the lowest excitation Strouhal numbers. Though nearly a direct inverse from the waveform observed in the irrotational near field, the far-field waveform is quite reminiscent of the phase-averaged waveforms observed by Kambe & Minota⁷ for the acoustic radiation towards aft angles produced by the head-on collision of vortex rings. At higher St_{DF} , a continuous oscillation between sharp expansion and compression waves is again observed, and again the amplitude begins to decay above moderate excitation Strouhal numbers.

A linear superposition of the impulse response can well predict the waveform shape and amplitude at the higher excitation frequencies (Fig. 29b), though in this case only up to $St_{DF} = 0.25$. From the phase-averaged waveforms alone it is not clear whether this breakdown in the linear superposition model at the

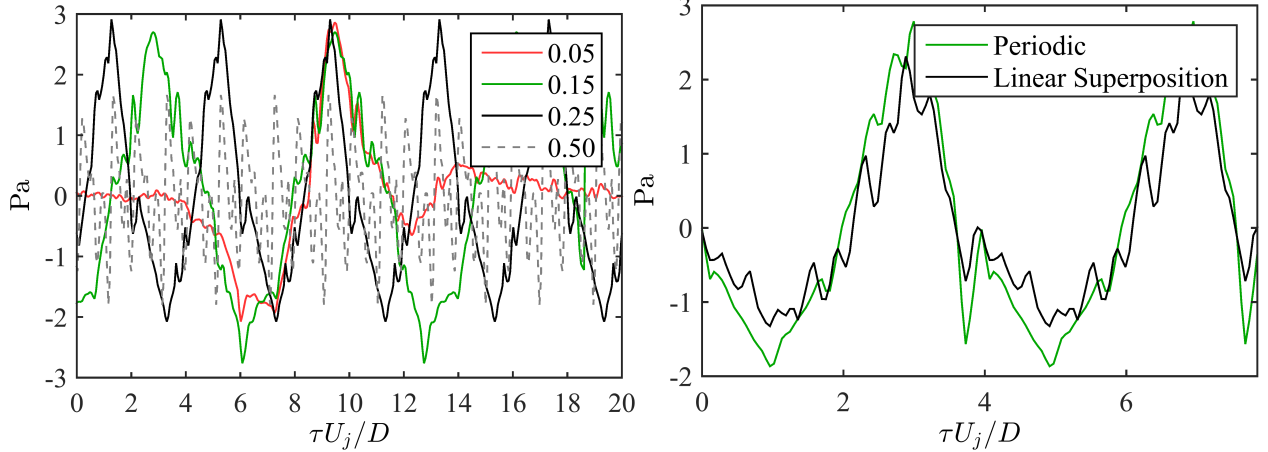


Figure 29: Phase-averaged waveforms of the far-field at 30° (a) and a linear superposition of the phase-averaged waveform for the impulse excitation ($St_{DF} = 0.05$) compared against periodic excitation ($St_{DF} = 0.25$) (b).

highest excitation frequencies is due to nonlinear behavior or uncertainty in the phase-averaging. The phase-averaged waveforms were also investigated at polar angles of 60° and 90° ; however a clear waveform was not identifiable over the statistical uncertainty inherent in the phase-averaging process (likely due to the superdirective character of the acoustic radiation,¹⁰ which renders the amplitude at sideline angles too low to be detectable).

III.E.2. Correlating the Near-Field and Far-field

Similar to the analysis of the numerical results, two-point linear correlations were computed between the near-field microphones and the far-field (in this case, from the far-field microphone at 30°), and analyzed in spatio-temporal domain along a single microphone array position. Correlations computed using the full near-field pressure are shown in Fig. 30, where the two-point correlations between the near-field and the far-field at 30° for two microphone array positions (starting at $x/D = 1, r/D = 1.20$ and $x/D = 1, r/D = 4.20$) have been plotted. Near the jet shear layer, four distinct correlation regions can be observed. The first group of correlation regions are noticeable beginning at the most upstream microphone and reach their peak values around $5 < x/D < 10$, decaying significantly beyond that. The slopes of these regions indicate propagation velocities noticeably below the sonic velocity; in the upstream region, they roughly match with the measured convective velocity of the large-scale structures ($U_c \simeq 0.7U_j$, and decelerate downstream). Conversely, the correlation regions dominant in the downstream region exhibit propagation velocities that match well with the ambient speed of sound.

As the microphone array is moved radially outwards, the upstream correlation regions quickly decay to negligible values and all observable correlation regions begin to match the expected time-of-arrival for sonically-traveling waves. The distinctly different propagation velocities and axial and radial evolutions of the two pairs of correlation regions indicate that these correspond to different physical phenomena. The upstream correlation regions observed near the jet shear layer are associated with the large-scale structures themselves, rather than acoustic phenomena, and their presence suggests a linear transfer of energy from the hydrodynamic to the acoustic field. The two-point correlations in the excited jet cases show similar behavior, albeit with enhanced correlation levels particularly for the large-scale structure related regions.

Therefore, in order to identify the source region of the acoustic fluctuations, the acoustic component of the near-field needs to be considered alone, rather than the full irrotational near-field pressure (Fig. 31). Gone entirely now are the correlation regions with subsonic propagation velocities, even at the closest microphone array positions. Instead, a single positive correlation region corresponding to sonically-propagating waves exists over the entire domain with significantly enhanced correlation over the full field results. It should be noted that the results found here for the acoustic component along the first microphone array position are nearly identical to those for the full field response at the further radial array positions (Fig. 30), which were

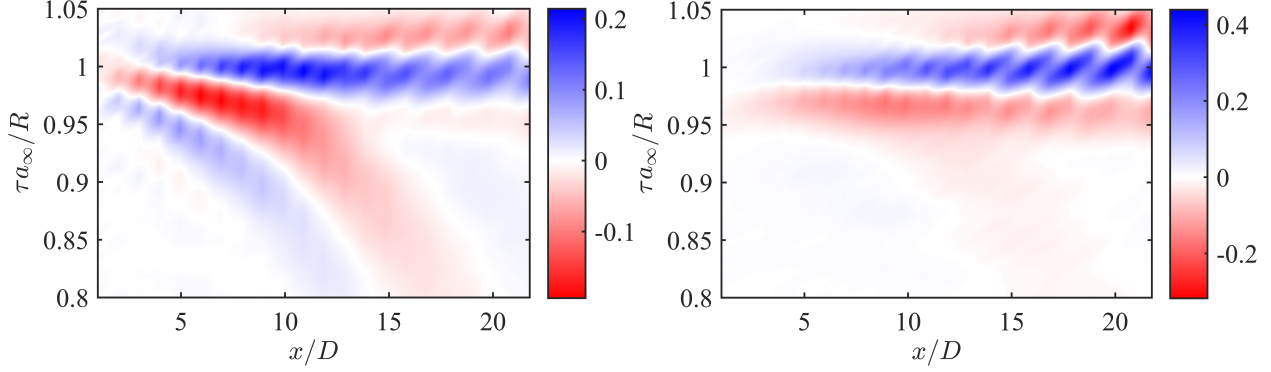


Figure 30: Normalized two-point correlations from the experimental results between the near field and the far field at 30° for (a) $r/D = 1.2$ and (b) $r/D = 4.2$.

dominated by acoustic, rather than hydrodynamic, energy.

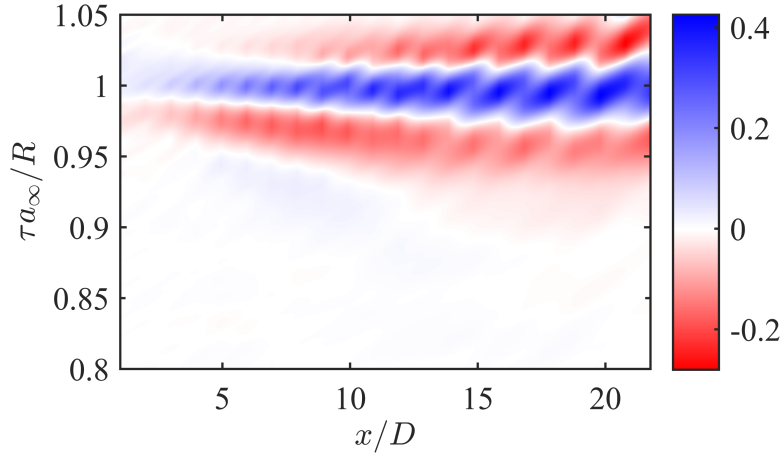


Figure 31: Normalized two-point correlations for the experimental jet between the acoustic component of the near field and the far field at 30° for microphone array position starting at $x/D = 1, r/D = 1.2$.

Similar behavior is observed between the natural jet and the excited cases in Fig. 32; note that due to numerical discrepancies at the domain boundaries (see Torrence & Campo⁵²), the correlation values have been truncated at the most upstream and downstream microphones. For the impulsively-excited jet, nearly identical correlation regions are observed between the excited and natural jet; in the periodically-excited jet continuous oscillations occur throughout time due to the similarity of continuously-generated large-scale structures and resultant acoustic radiation. In the upstream region of the jet, the peaks of the positive correlation region match τ_a nearly exactly. In the downstream region, τ_a begins to increasingly over-predict the time lag for the maximum correlation. On the other hand, τ_s tracks the time lags for the peak correlation consistently over the downstream region, but not the upstream region. The results found here appear to indicate that the dominant acoustic radiation reaching the far-field aft angles is being generated over an extended region of the jet mixing layer, roughly $x/D \leq 4$, which is just upstream of the time-averaged end of the potential core in the natural jet. This is not too dissimilar from the findings of other researchers, who have suggested that the acoustic source region lies just downstream of the end of the potential core.⁷ It should be clarified here though, that the interpretation of these results is not meant to suggest that only trivial levels of noise are generated outside of this apparent noise source region, just that the dominant radiation is produced in this region in a time-averaged sense.

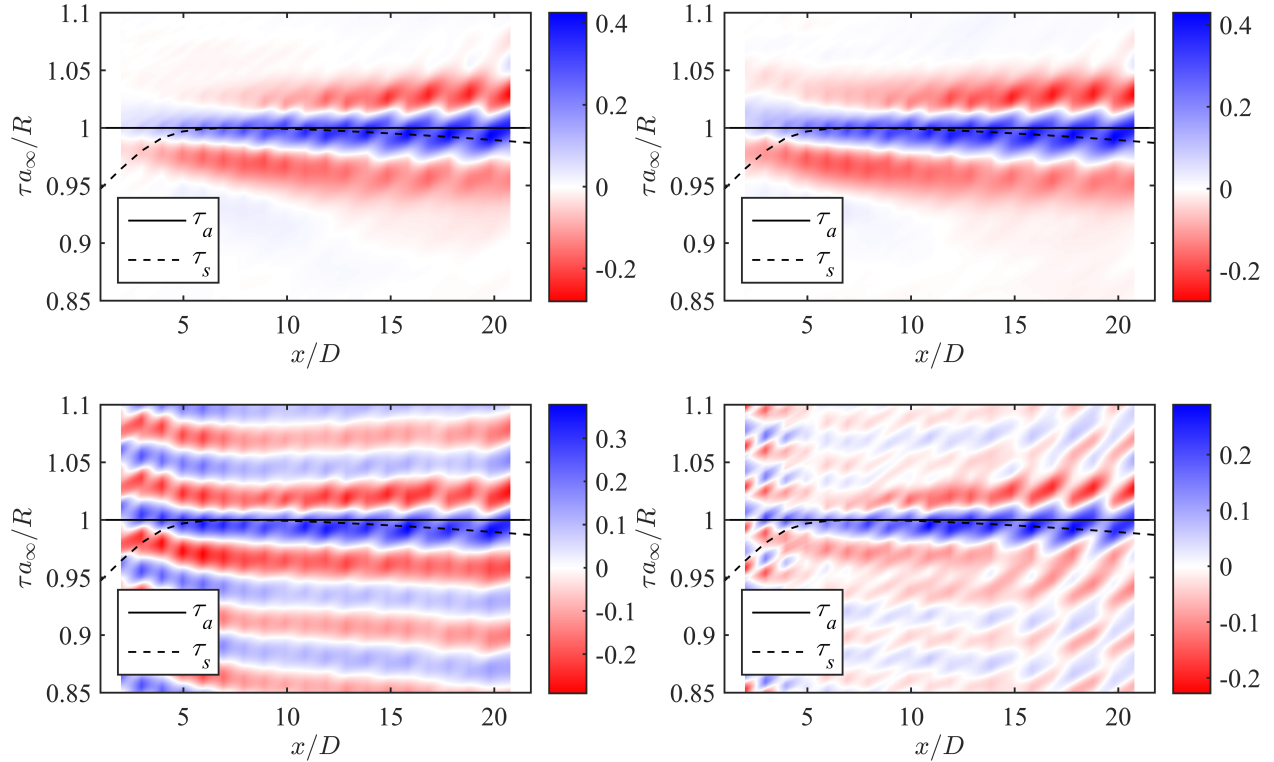


Figure 32: Normalized two-point correlations between the acoustic component of the near field and the far field at 30° for microphone array position starting at $x/D = 1, r/D = 1.2$ for the natural jet (a), $St_{DF} = 0.05$ (b), $St_{DF} = 0.25$ (c) and $St_{DF} = 0.35$ (d).

IV. Conclusions

An unheated, Mach 0.9 jet undergoing excitation with plasma actuators was analyzed using results obtained from experiments and computations to understand the large-scale structure dynamics, and ultimately the noise source mechanism and the resultant acoustic field. Previous experimental work by Sinha *et al.*¹⁷ had found that individual actuation events produce temporally and spatially localized pressure fluctuations in the irrotational near-field - the impulse response of the jet - and the response to periodic excitation could be reconstructed from a linear superposition of this impulse response. In this preliminary work, through the use of phase-averaging and Q-criterion iso-contours, analysis of the numerical results found that this same principle applied inside the jet shear layer (at the lipline), albeit with less accuracy; indicating that the structure interactions are largely (though not entirely) linear in nature. Results also showed that the near and far acoustic field are also governed by this quasi-linear mechanism at low to moderate frequencies ($St_{DF} \leq 0.25$) (though that is not to say that the noise generation process itself is necessarily linear).

Two-point correlations were then used to compare the irrotational near jet (hydrodynamically dominant) region to the acoustically dominant near and far fields. Results from both the experiments and simulations showed correlation regions matching the convection of the large-scale structures through the jet mixing layer. The full signal of the near field was decomposed into hydrodynamic and acoustic components via a linear filter utilizing a spatio-temporal wavelet transform, and correlations to the near and far acoustic field were recomputed. From these, the dependence of specific regions of the jet to the far field sound was characterized. It was found that the dominant noise source regions (insofar as they correlated best to the near and far acoustic field in a linear sense) comprised an extended region of the jet. However, results diverged between the experiments and simulations as to the exact length of this region. In the experimental jet, the natural as well as the excited cases all indicated that the dominant source region was near or upstream of the end of the potential core (roughly $x/D = 6$), as did the excited cases in the simulated jet. However, the natural jet in the simulated results indicated an apparent source region extended much further downstream, to roughly $x/D = 10$. The cause of this discrepancy, potentially the differences in the inlet flow (turbulent in the experiments and laminar in the simulations), is currently under further investigation.

Acknowledgments

Computational resources were provided by the DoD HPCMP (AFRL, NAVO and ERDC) and the Ohio Supercomputer Center. The support of this complementary experimental and computational work by the Air Force Office of Scientific Research (Dr. John Schmisseur and Dr. Rengasamy Ponnappan) is greatly appreciated. Several figures were made using Fieldview software with licenses obtained from the Intelligent Light University Partnership Program.

References

- ¹Wei, M. and Freund, J. B., "A noise-controlled free shear flow," *Journal of Fluid Mechanics*, Vol. 546, 2006, pp. pp. 123–152.
- ²Tam, C. K. W., Golebiowski, M., and Seiner, J. M., "On the Two Components of Turbulent Mixing Noise from Supersonic Jets," *AIAA/CEAS 2nd Aeroacoustics Conference*, Vol. AIAA Paper, State College, PA, May 6-8, 1996.
- ³Tam, C. K. W., "Directional acoustic radiation from a supersonic jet generated by shear layer instability," *Journal of Fluid Mechanics*, Vol. 46, No. 4, 1971, pp. pp. 757–768.
- ⁴Tam, C. K. W. and Burton, D. E., "Sound generated by instability waves of supersonic flows. Part 2. Axisymmetric jets," *Journal of Fluid Mechanics*, Vol. 138, 1984, pp. pp. 273–295.
- ⁵Panda, J. and Seasholtz, R. G., "Experimental investigation of density fluctuations in high-speed jets and correlation with generated noise," *Journal of Fluid Mechanics*, Vol. 450, 2002, pp. 97–130.
- ⁶Panda, J., Seasholtz, R. G., and Elam, K. A., "Investigation of noise sources in high-speed jets via correlation measurements," *Journal of Fluid Mechanics*, Vol. 537, 2005, pp. 349–385.
- ⁷Hileman, J., Carabalo, E., Thurow, B., and Samimy, M., "Large-Scale Structure Evolution and Sound Emission in High-Speed Jets: Real-Time Visualization with Simultaneous Acoustic Measurements," *J. Fluid Mech.*, Vol. 544, 2005, pp. 277–307.
- ⁸Sandham, N. D., Morfey, C. L., and Hu, Z. W., "Nonlinear mechanisms of sound generation in a perturbed parallel jet flow," *Journal of Fluid Mechanics*, Vol. 565, 2006, pp. 1–23.
- ⁹Cavalieri, A. V. G., Jordan, P., Gervais, Y., Wei, M., and Freund, J. B., "Intermittent sound generation and its control in a free-shear flow," *Physics of Fluids*, Vol. 22, No. 11, 2010, pp. 115113–.
- ¹⁰Crighton, D. G. and Huerre, P., "Shear-layer pressure fluctuations and superdirective acoustic sources," *Journal of Fluid Mechanics*, Vol. 220, 1990, pp. 355–368.

- ¹¹Samimy, M., Adamovich, I., Webb, B., Kastner, J., Hileman, J., Keshav, S., and Palm, P., "Development and characterization of plasma actuators for high-speed jet control," *Experiments in Fluids*, Vol. 37, No. 4, 2004, pp. 577–588.
- ¹²Utkin, Y., Keshav, S., Kim, J.-H., Kastner, J., Adamovich, I., and Samimy, M., "Use of Localized Arc Filament Plasma Actuators for High Speed Jet Control," *J. Phys. D: Applied Physics*, Vol. 40, Feb 2007, pp. 685–694.
- ¹³Samimy, M., Kim, J.-H., Kastner, J., Adamovich, I., and Utkin, Y., "Active control of high-speed and high-Reynolds-number jets using plasma actuators," *J. Fluid Mech.*, Vol. 578, 2007, pp. 305–330.
- ¹⁴Samimy, M., Kim, J.-H., Kastner, J., Adamovich, I., and Utkin, Y., "Active control of a Mach 0.9 jet for noise mitigation using plasma actuators," *AIAA Journal*, Vol. 45, No. 4, 2007, pp. 890–901.
- ¹⁵Samimy, M., Kearney-Fischer, M., Kim, J.-H., and Sinha, A., "High-Speed and High-Reynolds-Number Jet Control Using Localized Arc Filament Plasma Actuators," *Journal of Propulsion and Power*, Vol. 28, No. 2, 2012, pp. 269–280.
- ¹⁶Kearney-Fischer, M., Kim, J.-H., and Samimy, M., "A Study of Mach Wave Radiation Using Active Control," *Journal of Fluid Mechanics*, Vol. 681, 2011, pp. 261–292.
- ¹⁷Sinha, A., Alkandry, H., Kearney-Fischer, M., Samimy, M., and Colonius, T., "The Impulse Response of a High-Speed Jet Forced with Localized Arc Filament Plasma Actuators," *Physics of Fluids*, 2013.
- ¹⁸Crawley, M., Sinha, A., and Samimy, M., "Near-field and Acoustic Far-field Response of a High-Speed Jet Forced with Plasma Actuators," *AIAA Journal*, Accept, awaiting publication.
- ¹⁹Speth, R. and Gaitonde, D., "Correlation of Near Field Pressure with Coherent Structures in an Excited Mach 1.3 Jet," *ASME 2013 Fluids Engineering Division Summer Meeting*, No. FEDSM2013-16495, 2013.
- ²⁰Speth, R. and Gaitonde, D., "Near Field Pressure and Associated Coherent Structures of Excited Jets," *4th Joint US-European Fluids Engineering Summer Meeting*, , No. FEDSM2014-21186, 2014.
- ²¹Hahn, C., *Design and Validation of the New Jet Facility and Anechoic Chamber*, Ph.D. thesis, The Ohio State University, Columbus, OH, 2011.
- ²²Kearney-Fischer, M., Kim, J.-H., and Samimy, M., "Control of a High Reynolds Number Mach 0.9 Heated Jet Using Plasma Actuators," *Physics of Fluids*, Vol. 21, No. 9, 2009.
- ²³Utkin, Y., Keshav, S., Kim, J.-H., Kastner, J., Adamovich, I., and Samimy, M., "Characterization of Localized Arc Filament Plasma Actuators Used for High-speed Flow Control," *AIAA Paper 2007-0787*, 2007.
- ²⁴Hahn, C., Kearney-Fischer, M., and Samimy, M., "On factors influencing arc filament plasma actuator performance in control of high speed jets," *Experiments in Fluids*, Vol. 51, No. 6, 2011, pp. 1591–1603.
- ²⁵Gaitonde, D. and Samimy, M., "Coherent structures in plasma-actuator controlled supersonic jets: Axisymmetric and mixed azimuthal modes," *Phys. Fluids*, Vol. 23, No. 9, 2011.
- ²⁶Speth, R. and Gaitonde, D., "Parametric Study of a Mach 1.3 Cold Jet Excited by the Flapping Mode Using Plasma Actuators," *Computers & Fluids*, 2013.
- ²⁷Vinokur, M., "Conservation Equations of Gasdynamics in Curvilinear Coordinate Systems," *J. Comp. Phys.*, Vol. 14, 1974, pp. 105–125.
- ²⁸Steger, J., "Implicit Finite-Difference Simulation of Flow about Arbitrary Two-Dimensional Geometries," *AIAA Journal*, Vol. 16, No. 7, July 1978, pp. 679–686.
- ²⁹Speth, R. and Gaitonde, D., "The Effect of Laminar Nozzle Exit Boundary Layer Thickness on a Mach 1.3 Jet With and Without Control," *42nd AIAA Fluid Dynamics Conference and Exhibit*, 2012.
- ³⁰Roe, P., "Approximate Riemann Solvers, Parameter Vectors and Difference Schemes," *Journal of Computational Physics*, Vol. 43, 1981, pp. 357–372.
- ³¹van Leer, B., "Towards the Ultimate Conservation Difference Scheme V, A Second-Order Sequel to Godunov's Method," *Journal of Computational Physics*, Vol. 32, 1979, pp. 101–136.
- ³²Pulliam, T. and Chaussee, D., "A Diagonal Form of an Implicit Approximate-Factorization Algorithm," *J. Comp. Phys.*, Vol. 39, No. 2, 1981, pp. 347–363.
- ³³Beam, R. and Warming, R., "An Implicit Factored Scheme for the Compressible Navier-Stokes Equations," *AIAA Journal*, Vol. 16, No. 4, 1978, pp. 393–402.
- ³⁴Bellan, J., "Supercritical (and Subcritical) Fluid Behavior and Modeling: Drops, Streams, Shear and Mixing Layers, Jets and Sprays," *Prog. Energy Combust. Sci.*, Vol. 26, 2000, pp. 329–366.
- ³⁵Speth, R. and Gaitonde, D., "Parametric Study of a Supersonic Jet Subjected to Plasma-based Flapping Mode Excitation," *AIAA Paper 2012-0901*, 2012.
- ³⁶Gaitonde, D., "Analysis of plasma-based flow control mechanisms through large-eddy simulations," *Computers and Fluids*, Vol. 85, 2013, pp. 19–26.
- ³⁷Cohen, J. and Wygnanski, I., "The evolution of instabilities in the axisymmetric jet. Part 2. The flow resulting from the interaction between two waves," *J. Fluid Mech.*, Vol. 176, 1987, pp. 221–235.
- ³⁸Crawley, M., Sinha, A., and Samimy, M., "Near-field Pressure and Far-field Acoustic Response of Forced High-Speed Jets," *52nd Aerospace Sciences Meeting*, 2014.
- ³⁹Kastner, J., Kim, J.-H., and Samimy, M., "A Study of the Correlation of Large-scale Structure Dynamics and Far-field Radiated Noise in an Excited Mach 0.9 Jet," *International Journal of Aeroacoustics*, Vol. 8, No. 3, 2009.
- ⁴⁰Bogey, C. and Bailly, C., "Influence of Initial Turbulence Level on The Flow and Sound Field of a Subsonic Jet at a Diameter-based Reynolds number of 10^5 ," *J. Fluid Mech.*, Vol. 701, 2012, pp. 352–385.
- ⁴¹Alkandry, H., Crawley, M., Sinha, A., Kearney-Fischer, M., and Samimy, M., "An Investigation of the Irrotational Near Field of an Excited High-Speed Jet," *51st AIAA Aerospace Sciences Meeting*, 2013.
- ⁴²R., C. and G., G., "Orthonormal wavelet decomposition of turbulent flows: intermittency and coherent structures," *Journal of Fluid Mechanics*, Vol. 348, 1997, pp. 177–199.
- ⁴³R., C. and G., G., "Wavelet decomposition and coherent structures eduction of low Re turbulent hot wire signals," *Applied Scientific Research*, Vol. 57, 1997, pp. 195–209.

- ⁴⁴G., G. and R., C., "Statistical analysis of local turbulent energy fluctuations," *Journal of Fluid Mechanics*, Vol. 382, 1999.
- ⁴⁵R., C., "Coherent Structures identification from wavelet analysis of particle image velocimetry data," *Experiments in Fluids*, Vol. 32, 2002, pp. 76–86.
- ⁴⁶G., G., M., C., and R., C., "Acoustic Identification of coherent structures in a turbulent jet," *Journal of Sound and Vibration*, Vol. 259, 2003, pp. 1037–1065.
- ⁴⁷Farge, M., "Wavelet Transforms and Their Applications to Turbulence," *Annual Review of Fluid Mechanics*, Vol. 24, 1992, pp. 395–457.
- ⁴⁸Arndt, R. E. A., Long, D. F., and Glauer, M. N., "The proper orthogonal decomposition of pressure fluctuations surrounding a turbulent jet," *Journal of Fluid Mechanics*, Vol. 340, 1997, pp. 1–33.
- ⁴⁹Coiffet, F., Jordan, P., Delville, J., Gervais, Y., and Ricaud, F., "Coherent structures in subsonic jets: a quasi-irrotational source mechanism?" *International Journal of Aeroacoustics*, Vol. 5, No. 1, 2006, pp. 67 – 89.
- ⁵⁰Tinney, C. E. and Jordan, P., "The near pressure field of co-axial subsonic jets," *Journal of Fluid Mechanics*, Vol. 611, 2008, pp. 175–204.
- ⁵¹Crawley, M. and Samimy, M., "Decomposition of the Near-field Pressure in a Forced Subsonic Jet," *20th AIAA/CEAS Aeracoustics Conference*, June 2014.
- ⁵²Torrence, C. and Compo, G. P., "A Practical Guide to Wavelet Analysis," *Bulletin of the American Meteorological Society*, Vol. 79, No. 1, 1998, pp. 61–78.